Study on Magnetic Oxide Films with Spinel Structure for Electronics Devices

エレクトロニクス素子に向けたスピネル型構造を有する磁性酸化物薄膜に関する研究

Nozomi Takahashi

Graduate School of Chemical Sciences and Engineering
Hokkaido University

2019

Contents

Chapter 1
Introduction

1.1. Characteristics of Magnetic Oxide Films with Spinel Structure

The spintronics field which utilizes the spin and charge of electron, has attracted much attention. Researchers has attempted to create new functions with spintronics in the fields of magnetic engineering, semiconductor engineering, optical and so on[1-3]. In particular, the tunnel magnetoresistance (TMR) effect is fundamental phenomena in the spintronics, which is the key technology of magnetic random access memory (MRAM) and reading head of the high density HDD[4,5].

In the spintronics field, ferrite materials with spinel structure have recently used as magnetic layer. For example, the cobalt ferrite ($CoFe_2O_4$) is magnetic insulator, which is used as a tunnel barrier in spin filtering devices[6]. In addition, the magnetite (Fe_3O_4) has spin polarization of 100% in Fermi level, which is investigated as magnetic electrode in magnetic tunnel junctions[7]. Fig. 1 is the ideal spinel structure. The unit cell of spinel structure is formed by 8 cubes. Oxygen atoms form a fcc lattice and cations occupy the interstitial tetrahedral and octahedral sites. 8 divalent cations and 16 trivalent cations are in a unit cell. There are three different structures of spinel, normal, inverse and mixed. They are distinguished as a function of the cations distribution on tetrahedral (A) position and octahedral (B) position. In the normal spinel structure, divalent cations only occupy A sites and trivalent cations only occupy

B sites. For example, $MgAl_2O_3$ and $CoCr_2O_4$ and so on have normal spinel structure. In the inverse spinel structure, divalent cations only occupy B sites and trivalent cations equally occupy A sites and B sites. For example, $NiFe_2O_4$, Fe_3O_4, $CoFe_2O_4$ and so on have inverse spinel structure. In the mixed spinel structure, divalent cations and trivalent cations randomly occupy the A sites and B sites, which is the combination between the normal spinel and the inverse spinel structure. For example, $(Mn, Zn)Fe_2O_4$ is the mixed spinel structure.

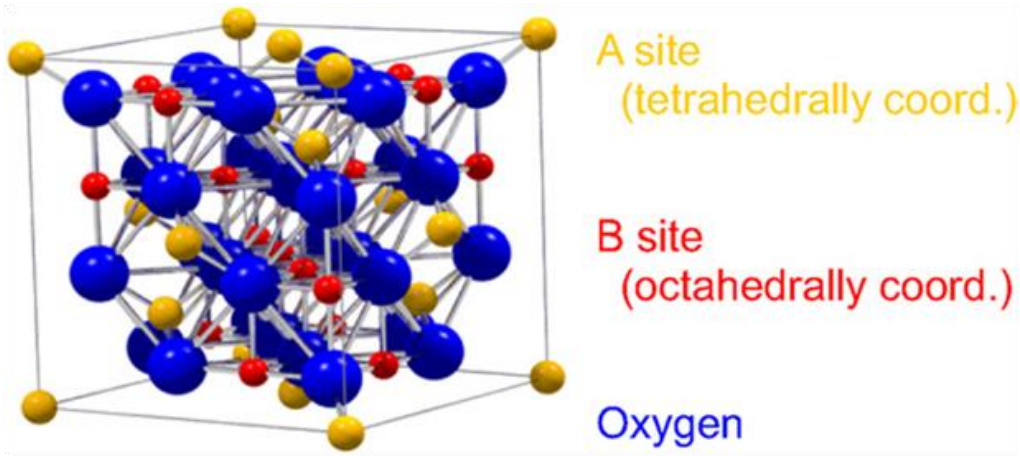

Fig. 1. Crystal structure of spinel[8]

As mentioned above, Fe_3O_4 is a kind of ferrites with inverse spinel structure. Although Fe_2O_3 is insulator, Fe_3O_4 has conductive property with 2.5×10^4 $\Omega^{-1} \cdot m^{-1}$ at room temperature. Fe_3O_4 also has Verwey transition at about 120 K. This transition was reported by E. J. W. Verwey[9]. The electrical conductivity of Fe_3O_4 is metallic at room temperature, and the resistance increases exponentially with decreasing temperature. At approximately 120K, the resistance increases drastically about two digits, called Verwey transition. Although the mechanism of Verwey transition has not been calrified in detail, it is considered to be due to the order-disorder transition of charge order

between Fe^{2+} and Fe^{3+}.

1.2. Half metal

The Fe_3O_4 is known as a half metal and attracts attentions as the material for spintronics devices[10,11]. Half metal is a ferromagnetic material in which the density of state of one spins is zero at the Fermi level, in other word, the spin polarization is 100%. The density of state of Fe_3O_4 which is calculated by first principle calculation is shown in Fig. 2 [12]. Only the DOS for ↑ spin exists near the Fermi level. This is called as the half metallic property, which is very attractive characteristics for spintronics devices. There are some candidates as half metallic materials; not only Fe3O4 but also Heusler alloy, CrO2, $La_{0.7}Sr_{0.3}MnO_3$(LSMO), which are confirmed by first principle calculation [13-15].

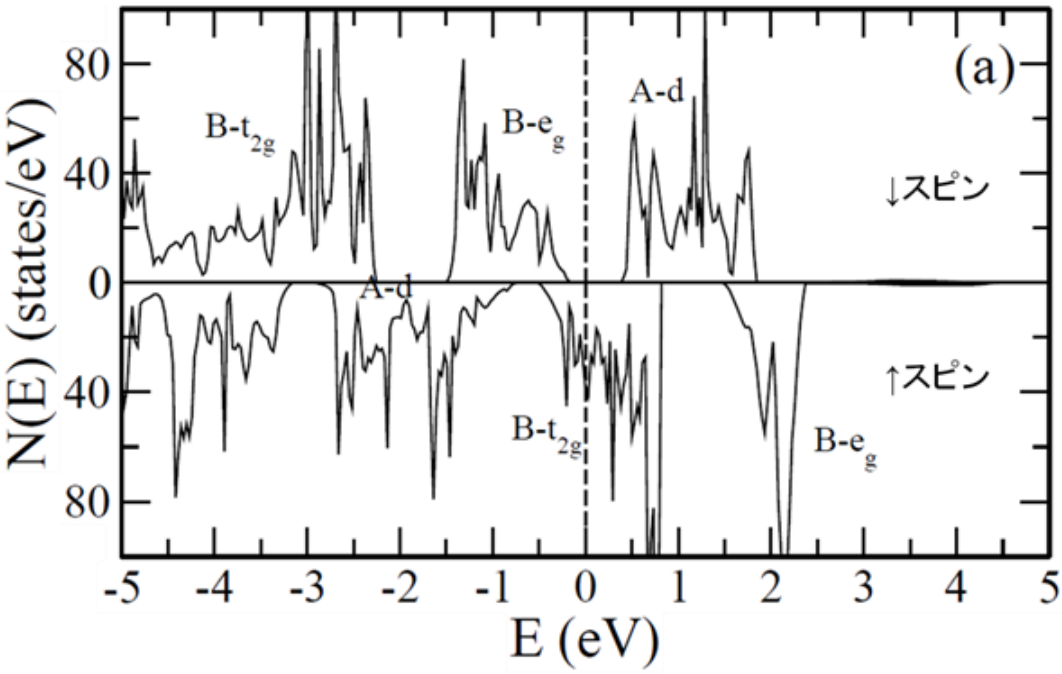

Fig. 2. The density of states of Fe_3O_4 by the first principle calculation[12].

1.3. Problems for Device Application

The magnetic oxide films with spinel structure are fabricated by a vacuum apparatus, then the quality of the thin film depends on the film forming rate, the film forming temperature, the annealing temperature, and the amount of introduced oxygen. In the case of preparing the magnetic oxides on substrates, it is necessary to obtain epitaxial thin films because the crystal grain boundary affects the magnetism and electron spin conduction of the material. Further, when the oxide films are used as electronic devices, it is conceivable to prepare electrodes in the upper layer. Therefore, it is preferable to be a thin film with good flatness.

Furthermore, when used as electronics materials, magnetic oxides with spinel structure is generally prepared on oxide substrates such as MgO, $SrTiO_3$, $MgAl_2O_4$, Al_2O_3 and so on[16-19]. However, since these oxide substrates are expensive, it is difficult to use them in large quantities in research and development, and it is desired to fabricate them by using inexpensive substrates. A silicon (Si) substrate has a diamond structure and has semiconductor properties and is used as a substrate. However, the crystal structure of silicon is different from the spinel type structure of Fe_3O_4 or $CoFe_2O_4$, and the mismatch of the lattice constant is about 3%.

It is also known that Si is one of a highly oxidizable material. Therefore, there is concern that the surface of the substrate may be oxidized at the time of preparing the magnetic oxide just above Si substrate (Fig. 3). Oxidation affects the epitaxial growth of the thin film, and also affects the electrical conductivity.

From the viewpoint of fabricating multilayer films for electronics devices, the method for fabricating thin films on the upper part has a more difficult condition than the lower layer. This is because the interface becomes rough by increasing the amount of

introduced oxygen or increasing the annealing temperature for fabricating the upper layer collapses. It is one of problems in selection of materials for electronics elements.

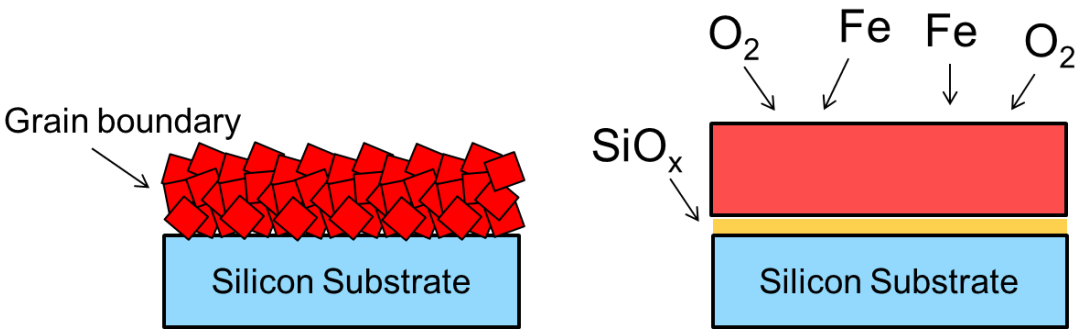

Fig. 3 Oxidation of Silicon Substrate under Magnetic Oxide Film

1.4. Objectives of Thesis

As mentioned above, although magnetic oxides with spinel structure attract attention as spintronics materials, there are various problems in fabricating techniques. In this thesis, I proposed the new method of quality improvement and the multilayers including spinel oxides by using the molecular beam epitaxy method.

Firstly, I fabricated the epitaxial Fe_3O_4 film on silicon substrates. In order to improve the quality of spinel oxides, I inserted a γ-Al_2O_3 ultarthin film as a buffer layer between Fe_3O_4 and Si substrates. The crystallization of the sample was investigated with 5-axis XRD and HR-STEM observation. In addition, I prepared the magnetic tunnel junctions with Fe_3O_4 as a magnetic electrode and investigate the magnetoresistance effect. I discussed the relation between the transport properties and the layer structure using the cross sectional TEM images.

Secondary, I fabricated multilayer films including spinel oxides in magnetic tunnel junctions based on the structure proposed by Slownczewski in 2011 [20]. The influences of the spinel oxide layers in the transport properties were investigated.

1.5. Construction of Thesis

This thesis consists of 6 chapters and organized as follows. In chapter 1, the introduction and purpose of this study are described.

In chapter 2, the epitaxial Fe_3O_4 films are fabricated on Si substrate. The γ-Al_2O_3 is inserted as a buffer layer between Fe_3O_4 and Si substrate because the lattice constant of γ-Al_2O_3 is matched to that of Fe_3O_4. Both γ-Al_2O_3 and Fe_3O_4 had an epitaxial crystal structure. Conversely, the Fe_3O_4 films on an amorphous-Al_2O_3 buffer layer that was grown at room temperature grew uniaxially in the (111) orientation and had a textured structure in the plane. This result suggested that the γ-Al_2O_3 buffer layer plays an important role for the formation of the epitaxial Fe_3O_4 film.

In chapter 3, the magnetic tunnel junction is fabricated on Si substrate. The sample structure was Si(111)/γ-Al_2O_3/Fe_3O_4/amo-Al_2O_3/Fe/Co/Au. The magnetoresistance of Fe_3O_4/amo-Al_2O_3/Fe is 2.5%, which is smaller than general magnetic junctions with Fe_3O_4. The anti-phase boundary and rough surface of Fe_3O_4 are considered to result in the small TMR ratio.

In chapter 4, the epitaxial growth and magnetoresistance of MTJs with spinel ferrite were investigated. Non-magnetic (NM) layers were inserted between the MTJs and spinel ferrite layers as magnetic decoupling layers, the epitaxial growth of which was important to obtain high-quality epitaxial multilayers. The shape of the magnetoresistance (MR) curve depended on the layer structures.

In chapter 5, the main conclusions of this thesis are summarized.

Reference

[1] A.Hirohata and K. Takanashi, J. Phys. D: Appl. Phys. 47, 193001 (2014).

[2] S. Datta, B. Das, Appl. Phys. Lett. 56, 665 (1990).

[3] Gyung-Min Choi, Byoung-Chul Min, Kyung-Jin Lee, David G. Cahill, Nature communications 5, 4334 (2014).

[4] S. Yuasa, T. Nagahama, A. Fukushima, Y. Suzuki and K. Ando, Nat. Mater. 3, 868 (2004).

[5] S. S. P. Parkin, C. Kaiser, A. Panchula, P. M. Rice, B. Hughes, M. Samant, S. Yang, Nat. Mater. 3, 862 (2004).

[6] Y. K. Takahashi, S. Kasai, T. Furubayashi, S. Mitani, K. Inomata, and K. Hono, Appl. Phys. Lett. 96, 072512 (2010).

[7] H. Matsuda, M. Takeuchi, H. Adachi, M. Hiramoto, N. Matsukawa, A. Odagawa, K. Setsune, H. Sakakima, Jpn. J. Appl. Phys. 41, 387-390 (2002).

[8] M. Opel, J. Phys. D., Appl. Phys. 45, 033001 (2012).

[9] E. J. W. Verwey and P. W. Haayman, Physica., 8, 979-987 (1941).

[10] G. Hu, Y. Suzuki, Phys. Rev. Lett. 89, 276601 (2002).

[11] T. Nagahama, Y. Matsuda, K. Tate, S. Hiratani, Y. Watanabe, T. Kawai, N. Takahashi, T. Yanase, T. Shimada, Appl. Phys. Lett. 105, 102410 (2014).

[12] P. L. Piekarz, A. M. Ole´s, and K. Parlinski, Institute of Nuclear Physics, Polish Academy of Sciences, Radzikowskiego 152, 31-342 (2010).

[13] F. Heusler, Verh. Dtsch. Phys. Ges. 5, 219 (1903).

[14] H. Tanaka, J. Zhang, T. Kawai, Phys. Rev. Lett. 88, 027204 (2002).

[15] J. M. De Teresa, A. Barthelemy, A. Fert, J. Contour, F. Montaigne, P. Seneor, Science 286, 507 (1999).

[16] H. Yanagihara, K. Uwabo, M. Minagawa, E. Kita, and N. Hirota, J. Appl. Phys. 109, 07C122 (2011).

[17] F. Rigato, J. Geshev, V. Skumryev, and J. Fontcuberta, J. Appl. Phys. 106, 113924 (2009).

[18]S. A. Krasnikova, A. S. Vinogradov, K. –H. Hallmeier, R. Höhne, M. Ziese, P. Esquinazi, T. Chassé, R. Szargan, Mater. Sci. and Eng. B 109, 207 (2004).

[19] M. Takahashi, T. Ohshima, H. Yamahara, M. Seki, and H. Tabata, J. Appl. Phys. 116, 213907 (2014).

[20] J. C. Slonczewski, Phys. Rev. B 82, 054403 (2010).

Chapter 2
Fabrication of epitaxial Fe_3O_4 film on Si(111) substrate

The application of metal oxides in spintronics has recently attracted much attention. However, epitaxial spinel ferrite films are generally grown on oxide substrates. To combine metal oxide spintronics and semiconductor technology, I fabricated Fe_3O_4 films through epitaxial growth on a Si(111) substrate by inserting a γ-Al_2O_3 buffer layer. Both γ-Al_2O_3 and Fe_3O_4 had an epitaxial crystal structure. Conversely, the Fe_3O_4 films on an amorphous-Al_2O_3 buffer layer that was grown at room temperature grew uniaxially in the (111) orientation and had a textured structure in the plane. The magnetic character of the Fe_3O_4 film strongly depended on the γ-Al_2O_3 buffer layer.

2.1. Introduction

In the field of spintronics, spin injection and transport phenomena have attracted much attention owing to the possibility of producing novel functional devices[1]-[3]. In particular, the combination of spintronics and semiconductors is a promising technology for the development of the next stage of spintronic devices, e.g., spin-FET or logic devices[4]-[5]. The spin injection technique has been intensely investigated for the preparation of spintronic devices. The spin-polarized currents are injected from ferromagnetic metals into conventional semiconductor materials[2][3][6]. As a result, researchers have succeeded in nonlocal detection[7] or the observation of the Hanle effect[1], which demonstrate the spin state in the semiconductor; thus, the behavior of the spin current in the semiconductor can be determined [8]. Recently, graphene has also been the subject of spin injection because the spin diffusion length in such light elements is expected to be long owing to small spin–orbit interaction[9][10].

The source of the spin current plays an important role in obtaining high-efficiency spin injection. Magnetic oxides are one of the most promising spin source candidates. However, ferromagnetic metals have been used so far because of convenience during fabrication. Magnetic oxides possess unique properties[11]-[14]; they have a half-metallic state, which provides highly spin polarized current[15], and are magnetic insulators, which means that they could work as a spin filter tunnel barrier[16]-[18]. Therefore, the combination of magnetic oxides and semiconductors enables us to produce new functional devices. However, epitaxial growth of magnetic oxide on Si, which is the most important semiconductor, has not been established because the surface of Si is easily oxidized by the oxygen atmosphere during the evaporation of the magnetic oxides[19].

In this study, I grew Fe_3O_4 epitaxially on a Si(111) substrate by the insertion of an

ultrathin γ-Al_2O_3 buffer layer. Fe_3O_4 is expected to be half-metallic and theoretically have a spin polarization of 100% [15]; a spin polarization of more than 80% was observed experimentally using a spin-resolved photoemission microscope[20]. An ultrathin γ-Al_2O_3 layer was inserted to prevent surface oxidation of Si. γ-Al_2O_3 is an aluminum oxide with the same spinel structure as Fe_3O_4. The lattice constant of γ-Al_2O_3 is 7.91 Å, which is just two thirds of that of Si[21]. From the viewpoint of the crystal structure, Fe_3O_4 and γ-Al_2O_3 appears to grow on Si epitaxially.

γ-Al_2O_3 could be grown epitaxially on Si by one of two methods. Jung et al. formed a γ-Al_2O_3 layer by annealing an Al layer on protective Si oxide, which was carefully oxidized to be reduced by the Al layer[22]. Merckling et al. fabricated γ-Al_2O_3 by the deposition of an Al_2O_3 source under ultra-high vacuum[23]. It is difficult to optimize the oxidation of the Si layer and the thickness of Al film using the former method. In contrast, the latter method is simple if an ultra-high vacuum system is accessible.

In this study, the epitaxial γ-Al_2O_3 buffer layers were prepared using an ultra-high vacuum system and the Fe_3O_4 layer was fabricated by reactive molecular beam epitaxy. I investigated the crystal structure, magnetic and electric properties of the Fe_3O_4 layer on Si (111) with an epitaxial γ-Al_2O_3 buffer layer, an amorphous-Al_2O_3 buffer layer, and without a buffer layer. I fabricated high quality Fe_3O_4 films on Si (111) substrates. The buffer layer had a significant effect on the crystal structure of the Fe_3O_4 layers.

2.2. Experimental Section

2.2.1. Experimental method

Before deposition, the Si substrate was treated by the RCA method[24] and HF solution and annealed at 900°C under a vacuum of $<10^{-6}$ Pa[23]. The γ-Al_2O_3 buffer layer was formed by evaporating the Al_2O_3 source material at 900°C and annealing at 900°C for 30 minutes. In previous reports, γ-Al_2O_3 was grown at >850°C and under a vacuum of $<10^{-6}$ Pa[25]. The growth conditions I used for γ-Al_2O_3 were in the range of the report. In Si(111) / amo-Al_2O_3 / Fe_3O_4, the amo-Al_2O_3 was grown at room temperature under a vacuum of $<3\times10^{-6}$ Pa. Then, the Fe_3O_4 film was formed by reactive deposition at 300°C under a O_2 atmosphere of 4.0×10^{-4} Pa[26]. All the samples were fabricated under the same growth conditions to investigate the dependence of the quality of Fe_3O_4 films on the buffer layer. The epitaxial growth and crystal structure were confirmed by RHEED, XRD (Rigaku SmartLab (9 kW)), and TEM (FEI Titan3 G2 60-300). Cross-sectional samples for TEM were prepared by using conventional mechanical polishing and dimpling techniques[27]. The magnetic properties of Fe_3O_4 were measured by vibrating sample magnetometer (VSM) and the electrical properties were measured by DC measurements.

2.2.2. Molecular Beam Epitaxy Method (MBE)

Techniques of fabrication of thin films are usually categorized in two groups. One is Chemical Vapour Deposition (CVD), which uses materials reacting in their vapour phase[28][29]. The other is Physical Vapour Deposition (PVD), which uses physical process to extract atoms from a solid. In our work, the used process was Molecular Beam Epitaxy method (MBE) which is one of the PVD methods.

MBE is an ultrahigh vacuum deposition technique consisting on molecular evaporation

of the constituent elements from one or more effusion cells to a heated substrate. MBE growth is carried out under conditions of the thermodynamic equilibrium and is conditioned by the kinetics of the surface processes. The growth rate is typically less than 1ML/s and the surface of the film can be very smooth. MBE is applicable to the epitaxial growth of a wide variety of materials. The facility of MBE used in our study is illustrated in Fig. 1.

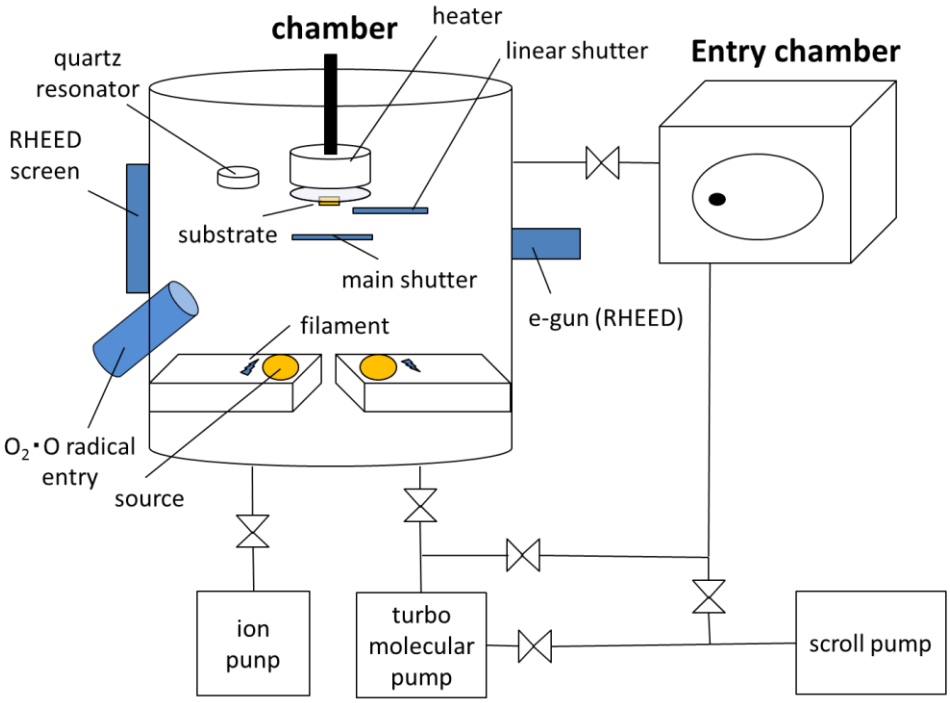

Fig.1. schematic of molecular beam epitaxy system

2.2.3. Diffraction Techniques

Diffraction by crystalline materials corresponds to the coherent scattering of X-rays or electrons by a periodic structure of atoms. It only occurs if the wavelength has the same order of magnitude as the periodicity of the structure probed.

A crystal is defined by its long order periodicity, with a repetition of its unit cell. This elementary volume "v" is defined in the real space by the base of vectors $\overrightarrow{a_1}, \overrightarrow{a_2}$ and $\overrightarrow{a_3}$,

as v = $\overrightarrow{a_1}(\overrightarrow{a_2}\wedge\overrightarrow{a_3})$. And atom positions can be described by: $\vec{R} = m_1\overrightarrow{a_1} + m_2\overrightarrow{a_2} + m_3\overrightarrow{a_3}$.

The reciprocal lattice is described with another vector base $\overrightarrow{b_1}, \overrightarrow{b_2}$ and $\overrightarrow{b_3}$. Where each vector is defined by par $\overrightarrow{b_i} = \frac{\overrightarrow{a_j}\cdot\overrightarrow{a_k}}{\overrightarrow{a_i}(\overrightarrow{a_j}\wedge\overrightarrow{a_k})}$, with i, j and k represent 1,2 or 3, and is orthogonal to two vectors of the direct base: $\overrightarrow{a_i}\cdot\overrightarrow{b_j} = 1$ if i = j, 0 if i $\neq$ j. $\vec{K}$ is then defined by $\vec{K} = h\overrightarrow{b_1} + k\overrightarrow{b_2} + l\overrightarrow{b_3}$, and more generally in the reciprocal lattice: $\overrightarrow{r^*} = n_1\overrightarrow{b_1} + n_2\overrightarrow{b_2} + n_3\overrightarrow{b_3}$.

A family of lattice planes are determined by the integers (hkl) called Miller indexes. Equivalently, (hkl) denotes a plane that intercepts the three points a_1/h, a_2/k, and a_3/l in the direct lattice. The vector $\vec{K}$ is orthogonal to the hkl planes , and its length is the inverse of the interplanar distance.

The radiation interaction with atomic planes of a crystal is shown in fig. 2, where the incident rays are diffracted with an angle of θ. In the real lattice, the condition of constructive interference is given by the Bragg law: 2dsinθ=nλ.

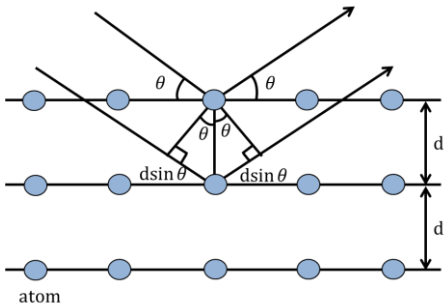

Fig. 2. The radiation interaction with atomic planes of a crystal

2.2.3.1. Reflection High Energy Electron Diffraction (RHEED)

Reflection High Energy Electron Diffraction (RHEED) consists in sending an accelerated electron beam in grazing incidence in the probed surface (up to 2°), and detecting the diffracted beams. This characterization technique reveals the crystallinity and roughness of the surface. In-situ RHEED can be combined with a deposition

technique, controlling the evolution of the thin film growth, from the first steps of the process. This is critical information to understand the growth mechanisms.

RHEED provides information about the periodic arrangement of the surface atoms, resulting in different types of patterns depending on the crystallinity and the surface morphology as shown in Fig. 3.

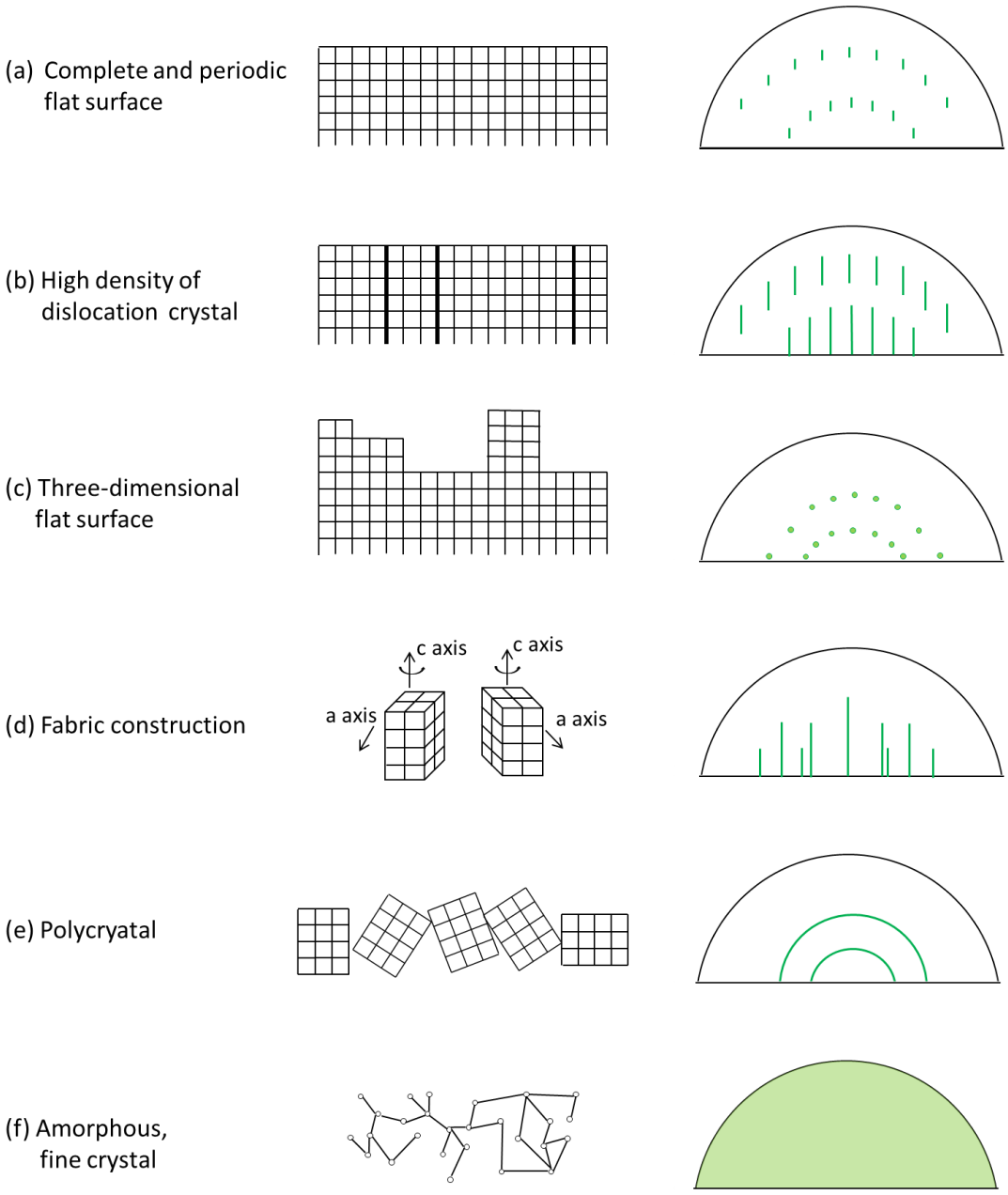

Fig. 3 Schematic of reflection high energy electron diffraction system

A diffuse halo is observed for amorphous surfaces, concentric rings for a polycrystalline state. For a single crystalline surface there is a pattern of Bragg spots along Laue circles. With moderate surface roughness, they transform to vertical streaks, but with high roughness arrays of spots characteristics of 3D diffractions appear.

2.2.3.2. X-ray Diffraction (XRD)

The wavelength of X-rays has the same order of magnitude that the interatomic plane distances. Then, interplanar distances can be detected from the theta angle (Bragg law), at which there is diffraction, and this permits to identify crystalline phases, orientation, and lattice strain in the analysed materials. In this thesis, Smart Lab (Rigaku) was used.

For an X-ray beam irradiating a set of crystallographic planes (hkl) the maximum intensity of the scattered beam occurs at an incidence angle according the Bragg law.

$$2d_{(hkl)} \sin\theta = \lambda$$

Where $d_{(hkl)}$ is the interplanar spacing, and λ is the wavelength of the used source of X-rays.

Two measurements geometries are presented in Fig. 4 : symmetric and asymmetric. In the symmetric configuration the diffraction planes are parallel to the sample surface, and in the asymmetric configuration the sample is oriented in order to obtain diffraction conditions for different planes non parallel to the sample surface.

The symmetric configuration θ-2θ adjustment is done with respect to the substrate. χ and ω are adjusted to obtain a substrate symmetrical reflection. The experimental substrate and film spectra in the symmetric configuration present different peaks corresponding to atomic planes parallel to the surface. The substrate, being typically perfectly crystalline and thick, shows high intensity and narrow peaks, while the width

of the film peaks is inversely proportional to spectra allows measuring the distance of the atomic planes in the direction perpendicular to the sample surface. In the case of textured films, a single family of planes is oriented perpendicular to the sample surface. In polycrystalline sample, different orientations can be observed in the spectra.

Other family planes tilted with respected to the sample surface can be measured with an asymmetric configuration of the system: ($\omega \neq 2\theta/\theta$, or tilting χ) and orienting properly the sample along the in-plane direction.

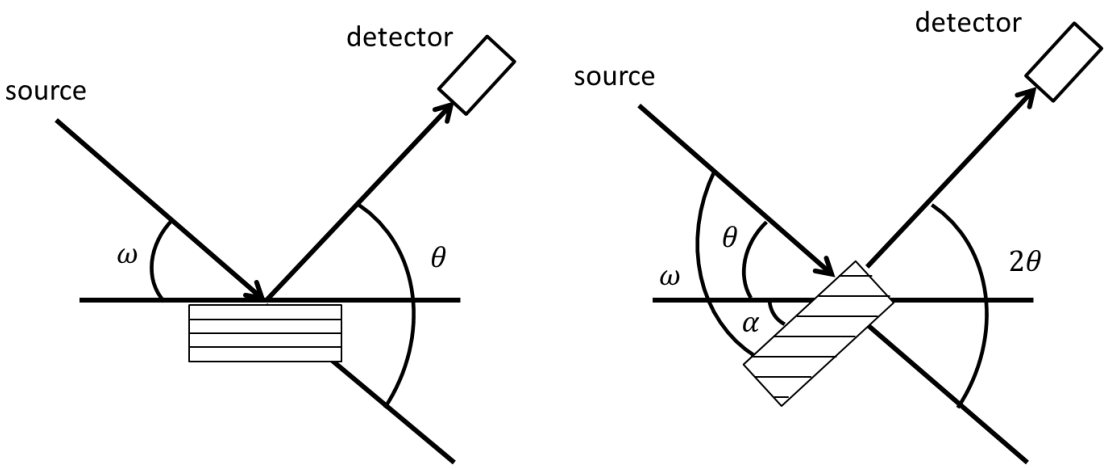

Fig. 4 symmetric configuration and asymmetric configuration

The ϕ-scans allow exploring the in-plane texture of the film by a sample rotation around the azimuthal angle ϕ. In order to satisfy the Bragg condition for a certain asymmetrical reflection, the sample is tilted in the χ angle while keeping the $\omega=\theta$ condition. This procedure allows determining the relative in-plane orientation between the film and the substrate and their epitaxial relationship. The combination of different θ-scan taken with different values of ω leads to a pole figure which is a 2-dimensional ϕ-ω map.

3.2.4. Observation of Flatness and Atomic Alignment by using Microscope

3.2.4.1. Atomic Force Microscope (AFM)

The atomic force microscope (AFM) permits to probe the surface topology, scanning with extremely high resolution (typically around 0.1 Å in the vertical direction, and from atomic resolution to some nm in the lateral direction). The AFM is composed by a tip hold in a cantilever which scans the sample surface as shown in Fig. 5. The normal forces exerted from the surface to the tip generate a cantilever deflection proportional to the force. A laser beam pointed on the cantilever is reflected in a photodiode detector with four panels, which measures the deflection during the scanning process. The characterization of the surface topography can be done in three different modes: contact mode, noncontact mode and tapping mode. The tapping mode was used in my study. The tapping mode, alternating the contact and noncontact modes, results to be a good compromise mode. The surface morphology of the samples studied in this thesis has been measured by tapping mode AFM.

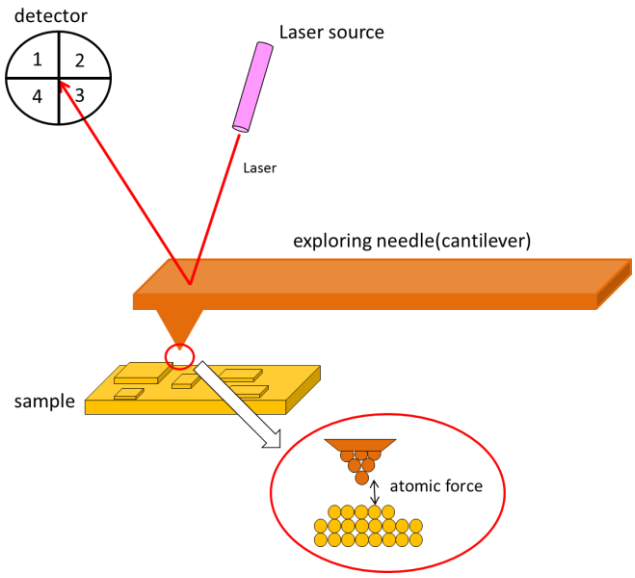

Fig. 5 Atomic force microscope system

3.2.4.2. Transmission Electrical Microscope (TEM)

Conventional TEM sample preparation

The conventional TEM sample preparation consist on a first mechanical thinning down process (grinder), and a precision ion polishing system (PIPS) to reach the electron transparency around the small hole. The preparation steps are shown for cross-section geometry in Fig.6, and described successively.

1. The specimen surface is carefully cleaned with solvent in order to obtain perfectly clean surfaces.
2. A thin glue film is spread over a surface, and a specimen-glue-specimen sandwich is formed when the two surfaces are put together face to face. This sandwich is introduced in a press in order to a very thin glue film. The whole mounting is placed in a furnace to ensure a proper glue polymerization. After polymerization, the glue should resist mechanical polishing and ion bombardment.
3. The sandwich or sample bock is then sliced into pieces around 1mm in thickness using a diamond abrasive saw.
4. The slice is glued on the sample holder and is wet polished using progressively finer lapping films until the scratches lines disappear. Then, the sample piece is turned the side, and is thinned down mechanically with progressively finer films until a thickness of around tens of microns, and then a copper grid is glued on it.
5. Ar ion bombardment focused on the middle of the sample thin it down to electron transparency.
6. At the edge of the hole, the sample is thin enough to be cross by accelerated electrons, and observable by TEM. At the electron microscope scale, the thin edges of the hole produced by the ion bombardment have parallel faces.

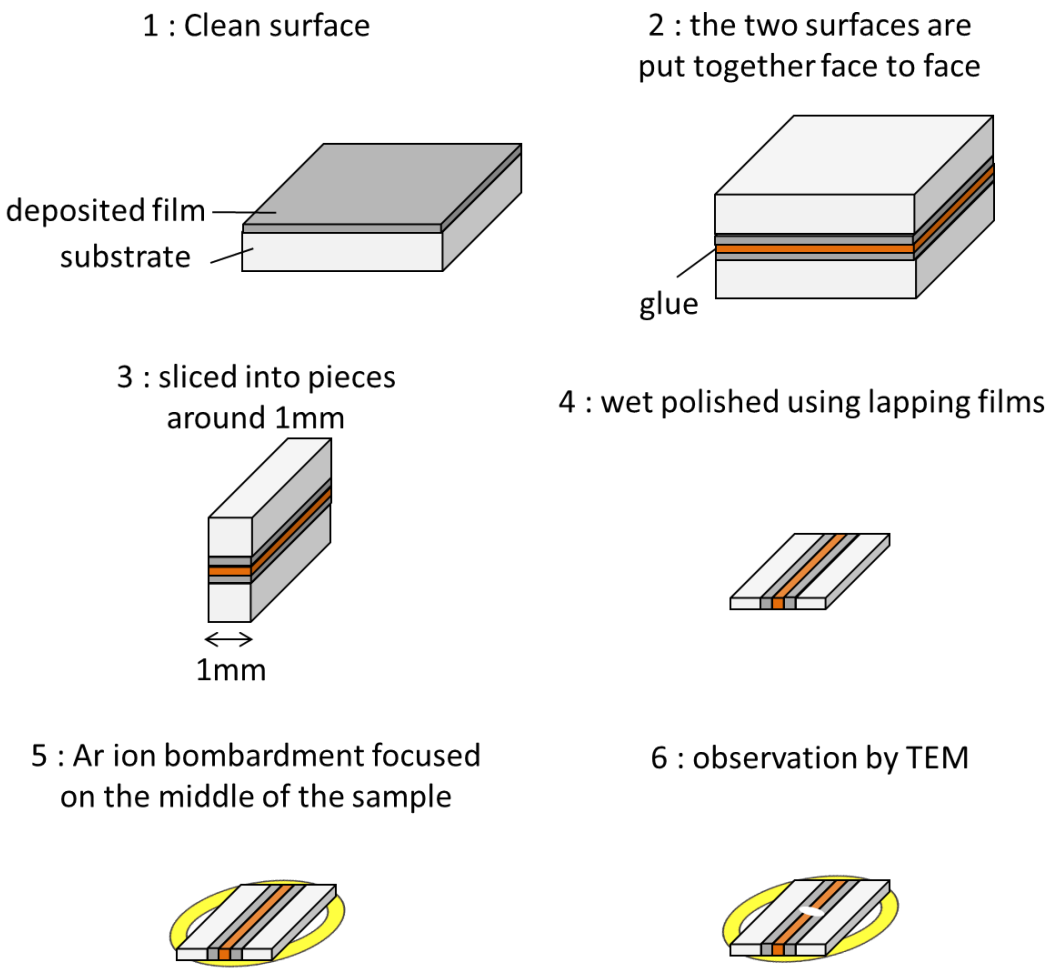

Fig. 6. Preparation procedure for cross-section geometry

2.3. Results and Discussion

2.3.1. Crystallization and Flatness by RHEED and AFM

The γ-Al_2O_3 and Fe_3O_4 layers were grown by molecular beam epitaxy. The structures of the samples were (a) Si(111) / γ-Al_2O_3 2.4 nm / Fe_3O_4 50 nm / amorphous-Al_2O_3 2.0 nm, (b) Si(111) / amorphous-Al_2O_3 2.4nm / Fe_3O_4 50nm / amorphous-Al_2O_3 2.0nm and (c) Si(111) / Fe_3O_4 50nm / amorphous-Al_2O_3 2.0nm, as shown in Fig. 7 (hereafter referred to as (a) EPI, (b) AMO and (c) W/O), respectively. After treatment of the Si substrate, I confirmed that the *in-situ* reflection high energy electron diffraction (RHEED) pattern

of the Si substrate had a 7×7 streak pattern (Fig. 8). This means that the surface of Si was clean and flat. Fig. 9 (a) and (b) show the RHEED pattern of γ-Al_2O_3 and Fe_3O_4 in EPI. The direction of the incident electron beam was [11-2]. The RHEED patterns of γ-Al_2O_3 and Fe_3O_4 were clear streak patterns. This indicated that γ-Al_2O_3 and Fe_3O_4 grew epitaxially; the γ-Al_2O_3 film was considered to play a role of a buffer layer for epitaxial growth of Fe_3O_4. The surface roughness of γ-Al_2O_3 and Fe_3O_4 were estimated to be very small in value by atomic force microscope (AFM) (Fig. 10).

Fig. 9 (c) and (d) show the RHEED pattern of amorphous-Al_2O_3 and Fe_3O_4 in AMO. The amorphous-Al_2O_3 layer was deposited at room temperature. After the deposition of Al_2O_3, as shown in Fig. 9 (c), the Si (7×7) streak pattern turned into a halo pattern, which indicated that the Al_2O_3 layer was amorphous. Fig. 9 (d) shows the RHEED pattern of Fe_3O_4 on the amorphous-Al_2O_3. A ring and streak pattern was observed, which implied the presence of a polycrystalline surface. Thus, the epitaxial γ-Al_2O_3 played a crucial role in the formation of epitaxial Fe_3O_4 on the Si substrate.

Fig. 9 (e) and (f) show the RHEED pattern of the Si substrate and Fe_3O_4 in W/O. The surface of the Si substrate exhibited a diffused streak pattern owing to the introduction of oxygen gas, which oxidized the Si surface. In Fig. 9 (f), the RHEED pattern of Fe_3O_4 on SiO_x shows a halo pattern, which indicated that spinel-type Fe_3O_4 was not formed.

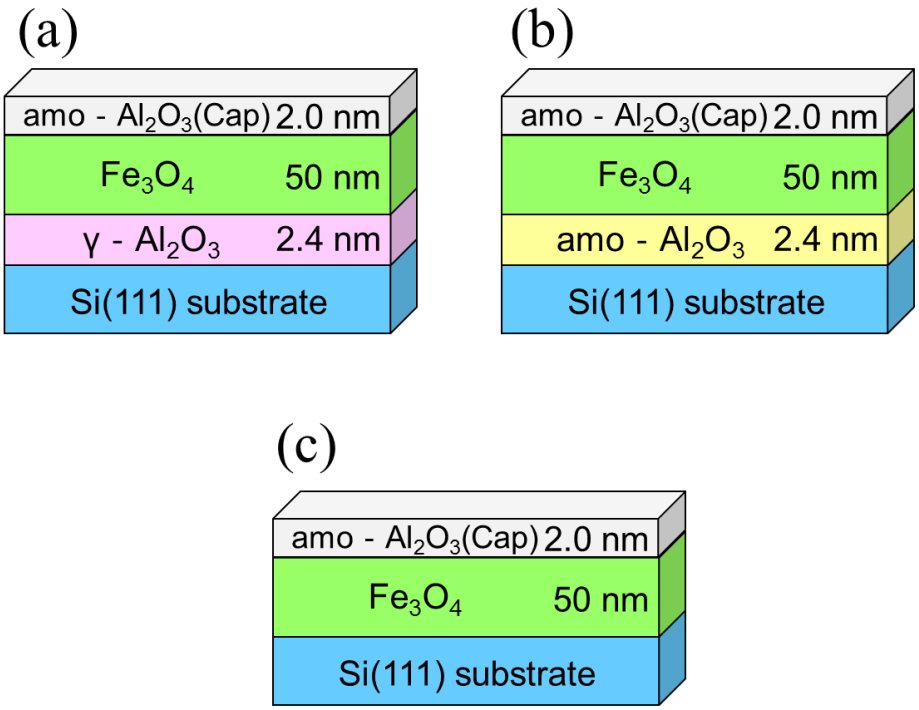

Fig. 7. Sample structures (a) the sample with γ-Al_2O_3 buffer layer, (b) with amorphous-Al_2O_3 buffer layer, and (c) without a buffer layer.

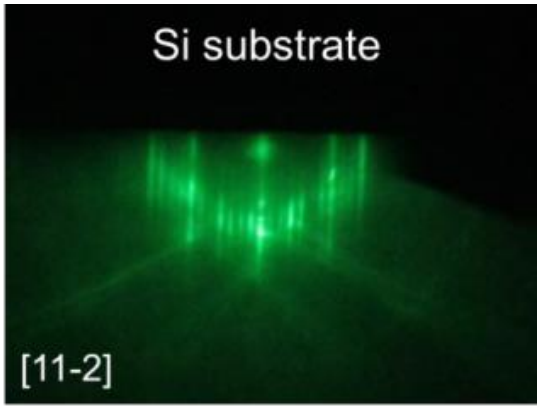

Fig. 8. RHEED pattern of the Si(111) substrate. The electron beam was along the [11-2] direction. The RHEED pattern was taken after the treatment and annealing. The RHEED pattern shows a clear 7×7 streak, which indicates that the oxidized silicon was removed.

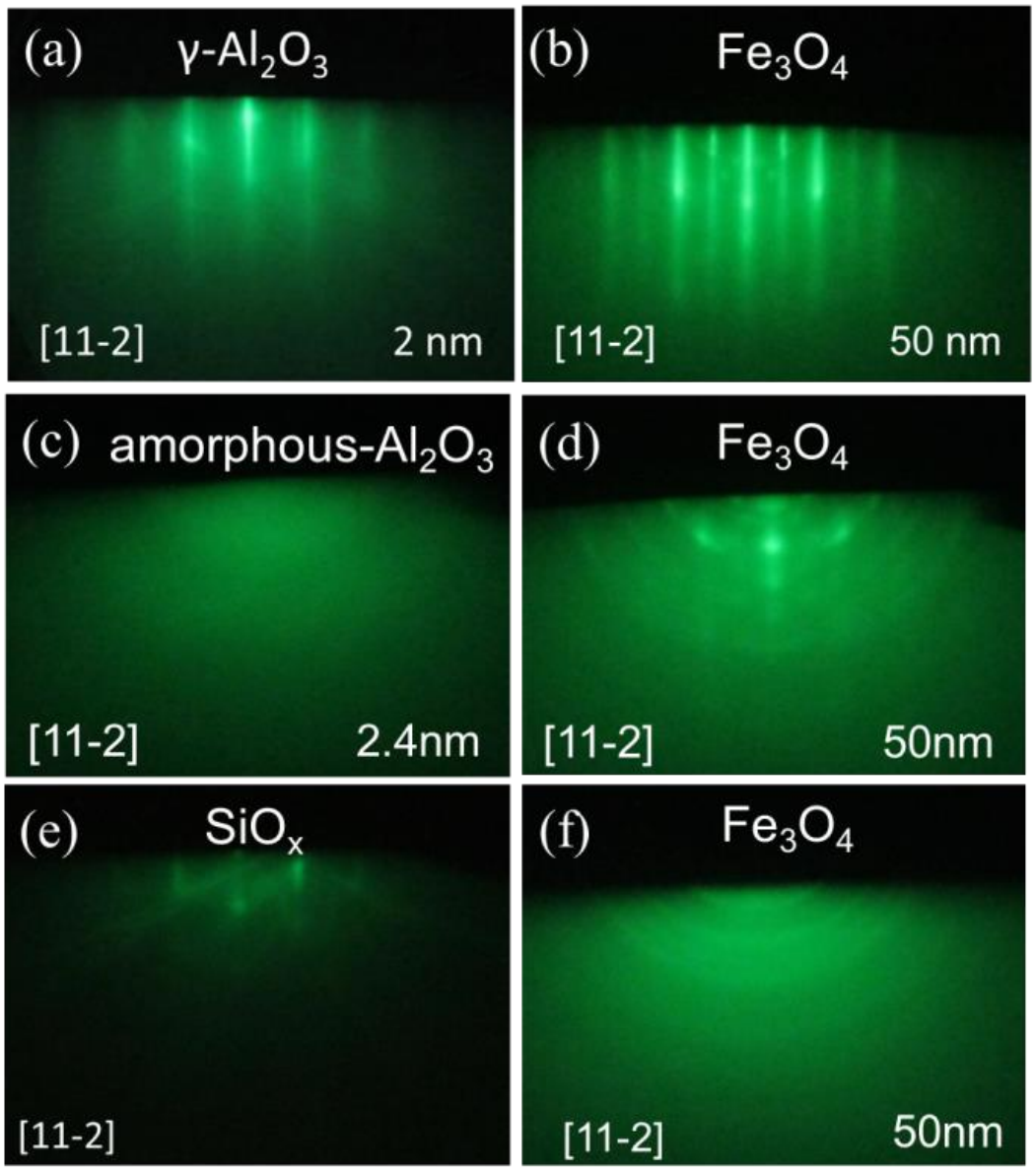

Fig. 9. RHEED patterns of (a) γ-Al_2O_3, (b) Fe_3O_4 film on γ-Al_2O_3, (c) amo-Al_2O_3, (d) Fe_3O_4 on amo-Al_2O_3, (e) Si surface before depositing Fe_3O_4, and (f) Fe_3O_4 on Si substrate

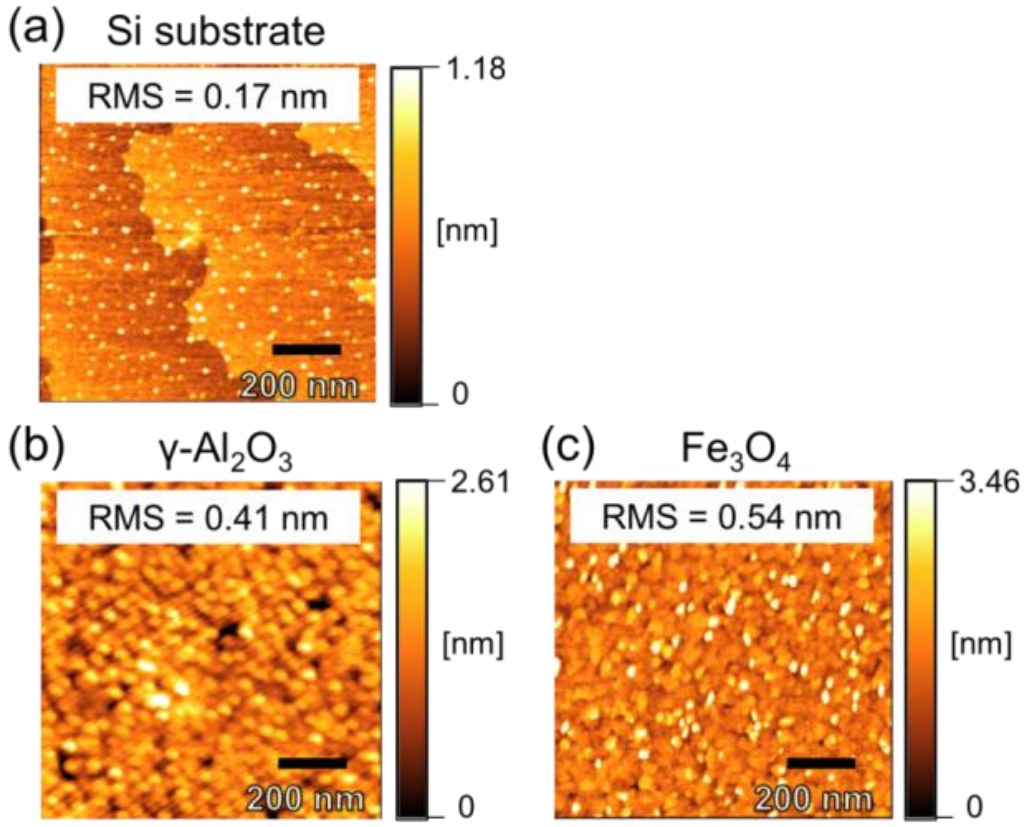

Fig. 10. AFM images of (a) Si, (b) γ-Al_2O_3 and (c) Fe_3O_4. The roughness of root mean square (Rrms) value of the Si substrate was estimated to be 0.17 nm (Fig. 10 (a)). The image has a terrace-and-step structure. The Rrms of γ-Al_2O_3 was estimated to be 0.41 nm (Fig. 10 (b)). The surface of the γ-Al_2O_3 film consists of grains, sized 40–50 nm. The Rrms of Fe_3O_4 was estimated to be 0.54 nm (Fig. 10 (c)). The grain size in Fig. 10 (c) was the same as that in Fig. 10 (b).

2.3.2. Crystallization of Fe_3O_4 Film by X-ray Diffraction

To confirm the crystallization, the θ–2θ X-ray diffraction (XRD) measurements were carried out on three samples, as shown in Fig. 11 (a). The diffraction pattern of Fe_3O_4 on an γ-Al_2O_3 buffer layer in EPI (red line) exhibited four peaks (18.3°, 37.2°, 57.2°, 79.4°), which were in agreement with the diffraction patterns of Fe_3O_4 (111), (222), (333) and

(444) planes. This indicated that the Fe_3O_4 film was (111)-oriented without other orientations or phases. The lattice constant measured by XRD was estimated to be 8.39 Å. The lattice constant of the in-plane direction was estimated to be 8.23 Å (Fig. 12), which is smaller than the bulk lattice parameter. Therefore, the Fe_3O_4 was considered to be compressed in-plane.

To investigate the in-plane epitaxial relationship, I conducted ϕ-scan measurements of Si (311) and Fe_3O_4 (4-40), as shown in Fig. 11 (b). The six peaks of Fe_3O_4 (4-40) appeared at 60° intervals, indicating the presence of two 180° rotated domains in the Fe_3O_4 layer. The epitaxial relationships were [11-2]Fe_3O_4(111) and [-1-12]Fe_3O_4(111) parallel to [11-2]Si(111), as exhibited in Fig. 9 (c). In addition, the peaks of the Fe_3O_4 film were broader than that of the Si substrate. There was a lattice mismatch of 5.7% at γ-Al_2O_3 / Fe_3O_4.

The θ–2θ XRD diffraction pattern of Fe_3O_4 in AMO (blue line) exhibited four peaks, which was identical with the diffraction pattern of Fe_3O_4 in EPI. Therefore, the Fe_3O_4 in AMO was also (111)-oriented. However, the RHEED pattern in Fig. 7 (d) implied the presence of a polycrystalline structure. Furthermore, the Fe_3O_4(4-40) diffraction peak was not observed in the ϕ-scan measurement. Therefore, I concluded that the Fe_3O_4 had a textured structure and the growth direction was (111).

The θ–2θ XRD diffraction pattern of Fe_3O_4 in W/O (green line) exhibited small peaks related to Fe_3O_4(311), (400), (422) and unknown peaks. In a previous study[30], the XRD of Fe_3O_4 on SiO_2 indicated that the Fe_3O_4 layer was polycrystalline and contained other phases.

To investigate the crystallinity of the Fe_3O_4 layer in detail, I carried out X-ray reciprocal space mapping around the symmetric (222) diffraction for Fe_3O_4 in EPI and AMO (Fig. 11 (d)). The symmetrical scan showed that the Fe_3O_4(222) spot on amorphous-Al_2O_3 was

larger than the Fe_3O_4 spot on γ-Al_2O_3, which means that the Fe_3O_4 in AMO had an angle distribution in the growth directions. Although the reason for the (111) oriented Fe_3O_4 growth on amorphous-Al_2O_3 / Si(111) was unclear, two possibilities exist that could explain this growth. The first is a reduction in the total anisotropy energy related to the surface energy and interface energy[31]. The difference between AMO and W/O could be attributed to the difference of the surface and interface energy of amo-Al_2O_3 and amo-SiO. The second possibility is that the amo-Al_2O_3 maintains a crystal structure of Si locally because the amo-Al_2O_3 layer was very thin. Fe_3O_4 could utilize such a microcrystal-like region as a growth nucleus.

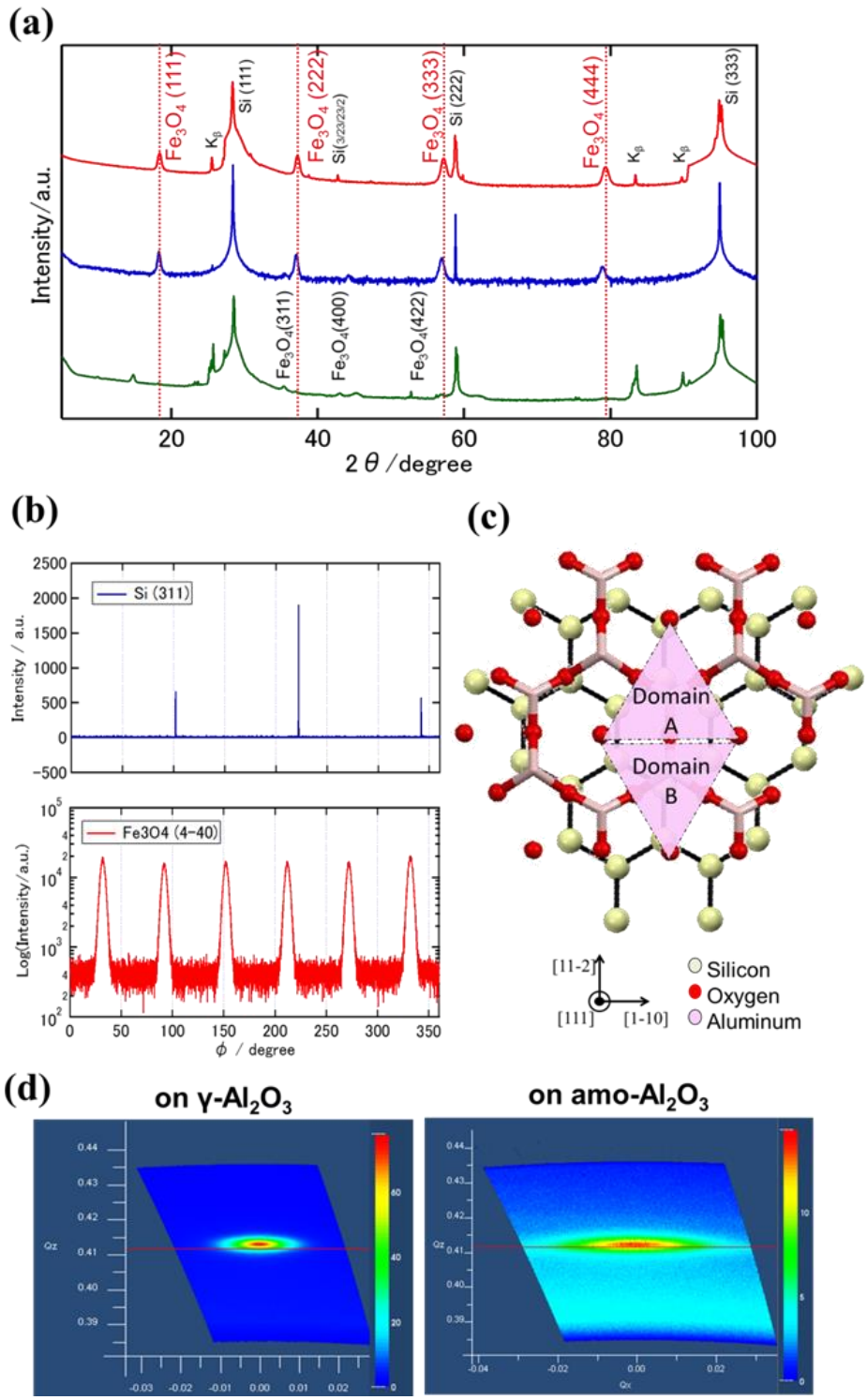

Fig. 11. (a) θ-2θ X-Ray diffraction profiles, (b) ϕ-scan measurement, (c) Epitaxial relationship between Si and γ-Al_2O_3, (d) X-ray reciprocal space maps of Fe_3O_4 on γ-Al_2O_3 and Fe_3O_4 on amo-Al_2O_3.

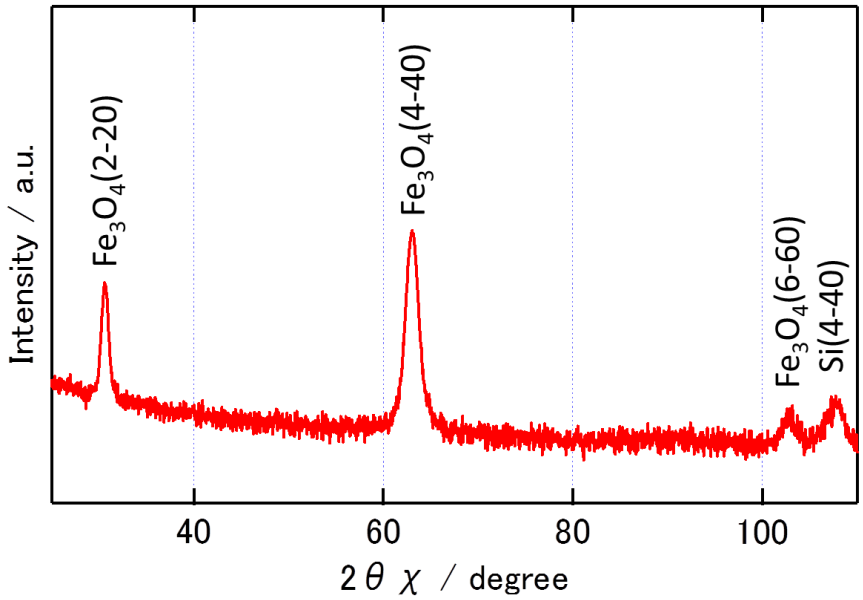

Fig. 12. In plane XRD profile of the Fe_3O_4 film. The in-plane X-ray diffraction profile for Si(111) / γ-Al_2O_3 / Fe_3O_4 exhibited three peaks (30.6°, 63.04°, 102.76°, respectively). They were assigned as the diffraction peaks of Fe_3O_4(2-20), (4-40) and (6-60), respectively, which indicated that the Fe_3O_4 film grew epitaxially on γ-Al_2O_3.

2.3.3. Observation of Interface by HRTEM

I conducted cross-sectional transition electron microscopy (TEM) analysis to confirm the crystallinity and compositions of the materials. Fig. 13 shows the cross-section TEM images in which the electron beams were incident along the Si [1-10] zone axis. In Fig. 13 (a), the TEM image shows that the Fe atoms of Fe_3O_4 were orderly aligned; thus, the Fe_3O_4 film was epitaxial. The electron diffraction (ED) of Fe_3O_4 in EPI shown in Fig. 13 (b) was in good agreement with the simulation of spinel structure. The left panel in Fig. 13 (a) shows the epitaxial relationship on [11-2]Fe_3O_4(111) / [11-2]Si(111), whereas the center panel shows the epitaxial relationship on [-1-12]Fe_3O_4(111) / [11-2]Si(111), which were consistent with the results of the ϕ-scan measurements in the XRD. In addition,

the spacing of the (111) planes were estimated at 4.87 Å from the high angle annular dark-field scanning (HAADF) image (Fig. 15 (c)), which were almost the same as the out-of-plane lattice constant (4.84 Å) determined by XRD in Fig. 11 (a) and that of bulk Fe_3O_4 (4.85 Å). In contrast, the TEM image of Fe_3O_4 in AMO shown in Fig.13 (c) demonstrated that the structure was polycrystalline and grain boundaries were clearly observed. The ED image in Fig. 13 (d) consisted of the diffraction from the grains with some crystal orientations. In the low magnification TEM image (Fig. 15 (b)), some grains with a size of 15–30 nm appeared.

With respect to the buffer layer, the thickness of γ-Al_2O_3 was estimated from the HRTEM image (Fig. 13 (a)) to be approximately 1 nm, which was thinner than the nominal value measured by the crystal oscillator in the chamber. The reason for this difference in thinness was unclear; however, it could be due to the fluctuation of the crystal oscillator or re-evaporation because the γ-Al_2O_3 was grown at a high temperature (900°C). I could see the amorphous layer under the γ-Al_2O_3 layer, which was determined to be a SiO_x layer by HAADF and EDS mapping images (Fig. 14). The SiO_x layer was considered to form during the growth of Fe_3O_4 because the Fe_3O_4 was grown in 4×10^{-4} Pa O_2 gas. It was reported that Si was oxidized through the γ-Al_2O_3 layer of less than 2.0 nm by introducing oxygen (>10^{-5} Torr) [32]. To confirm that, I fabricated a γ-Al_2O_3 (7.5 nm) film on Si (111), and carried out XRD and TEM observations (supplementary Fig. 16 (a) and (b)). The γ-Al_2O_3 grew epitaxially on Si and I found no amorphous layer at the Si(111) / γ-Al_2O_3(7.5 nm) interface.

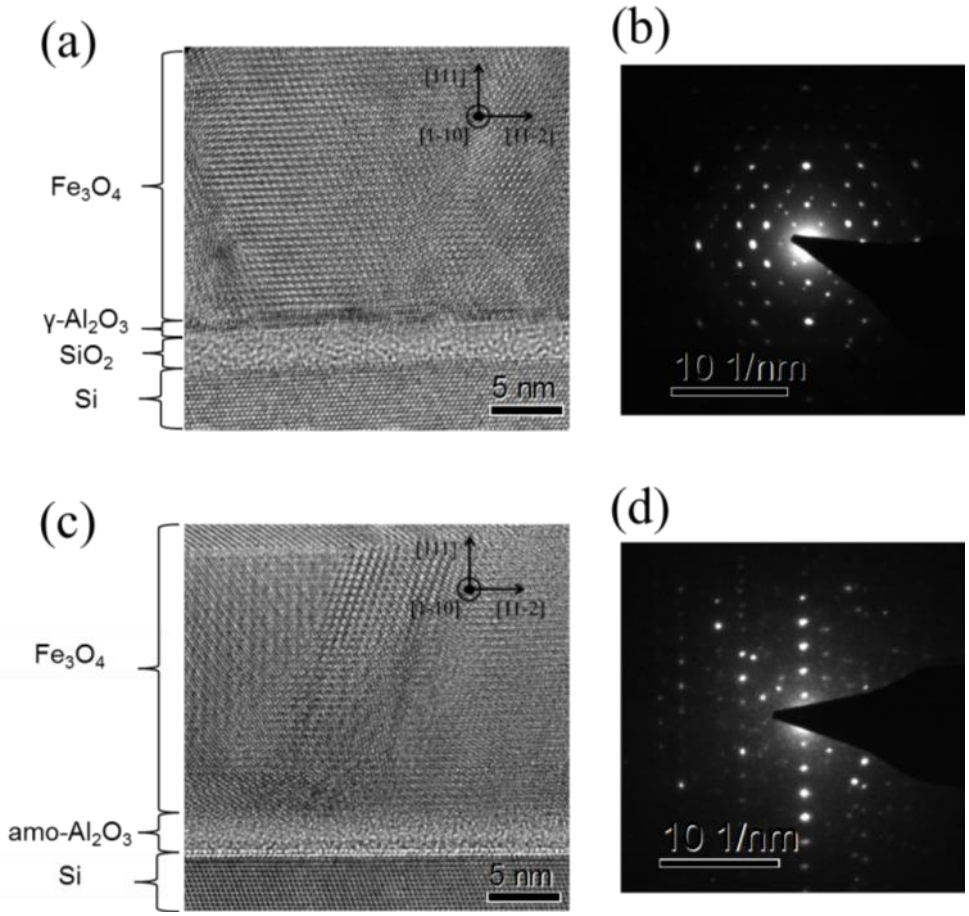

Fig. 13. (a)Cross-section TEM image and (b) electron diffraction pattern of Si(111) / γ-Al_2O_3 / Fe_3O_4 taken along the [1-10] axis zone, (c) Cross-section TEM image and (d) electron diffraction of Si(111) / amo-Al_2O_3 / Fe_3O_4 taken along the [1-10] axis zone.

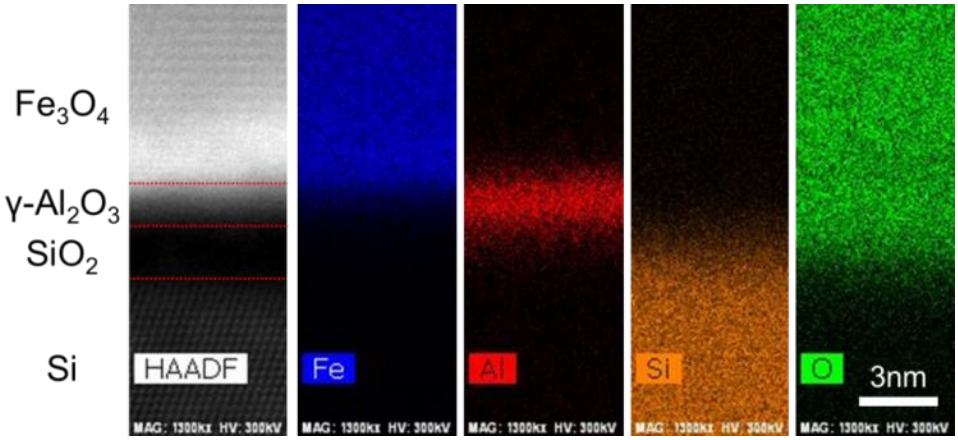

Fig. 14. The EDS mapping of the heterostructure: From the left image, HAADF image, EDS mapping of Fe, Al, Si, and O.

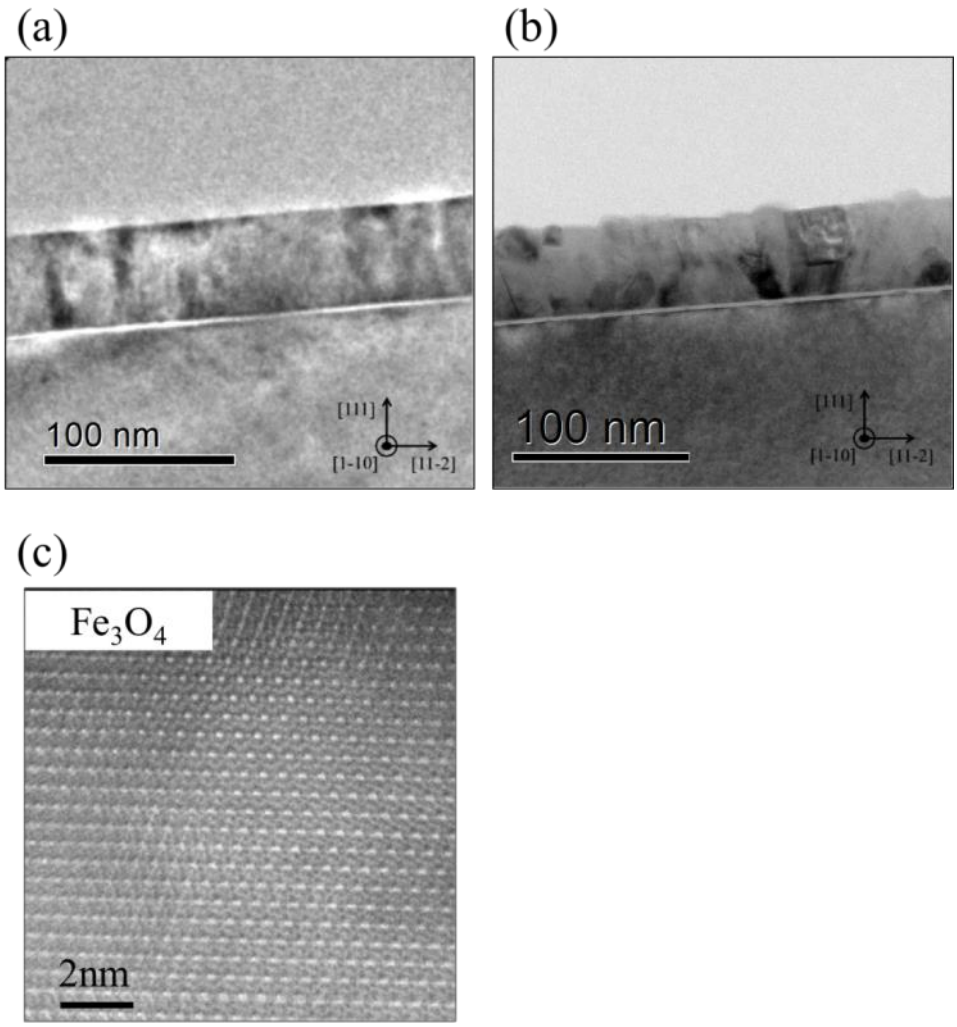

Fig. 15. TEM images of (a) Si(111) / γ-Al_2O_3 / Fe_3O_4 and (b) Si(111) / amo-Al_2O_3 / Fe_3O_4 heterostructure. (c) High resolution HAADF image of the Fe_3O_4 on γ-Al_2O_3 buffer layer. The TEM and HAADF images were taken along the [1-10] zone axis. The Fe_3O_4 film on a γ-Al_2O_3 buffer layer in Fig. 15 (a) was homogeneous, whereas grain boundaries were observed in the Fe_3O_4 film on amo-Al_2O_3, as shown in Fig. 15 (b). Fig. 15 (c) shows that the Fe atoms were aligned in an orderly manner. The intervals of the atoms corresponded to the Fe_3O_4 lattice parameter.

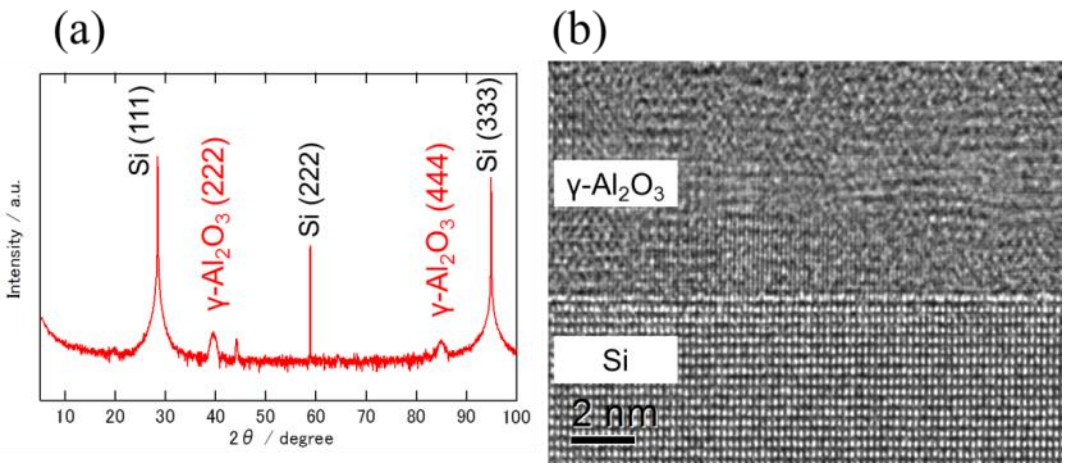

Fig. 16. (a) X-ray diffraction profile and (b) TEM image of Si(111) / γ-Al_2O_3 (7.5 nm) Fig. 16 (a) exhibited two peaks (39.58°, 84.92°) corresponding to the diffraction of γ-Al_2O_3(222) and (444), respectively, which indicated that the γ-Al_2O_3 film only had a (111) orientation and no other phases. Fig. 16 (b) was taken along the [11-2] zone axis. It showed that the γ-Al_2O_3 was a single crystal and the SiO_x did not exist at the interface of Si(111) / γ-Al_2O_3 (7.5 nm).

2.3.4. Magnetic Properties and Electrical Properties

The magnetic character of Fe_3O_4 is one of its fundamental properties. The magnetization curves at room temperature for the Fe_3O_4 films on γ-Al_2O_3 layer are shown in Fig. 17 (a). The directions of the magnetic field were in-plane [11-2], in-plane [1-10] and out-of-plane [111]. The hysteresis curve along [11-2] was the same as that along [1-10] and the Fe_3O_4 film had in-plane magnetization. The saturation magnetization (Ms) was 480 emu/cc for all magnetic field directions. The remanent magnetization (Mr), the coercive field (Hc), and the remanent ratio (Mr/Ms) in the in-plane field were 280 emu/cc, 500 Oe, and 0.48, respectively, and those for the out-of-plane field were 47 emu/cc, 225 Oe, and 0.08, respectively. The hysteresis loops for Fe_3O_4 in EPI, AMO, and W/O are illustrated in Fig.

17 (b). Fe_3O_4 in EPI had the largest Hc and Ms among the three samples. The Ms of Fe_3O_4 in EPI was the same as the value of bulk Fe_3O_4.

Fig. 19 shows that the dependence of the resistance on temperature for the Fe_3O_4 film in EPI. As is well-known, Fe_3O_4 is an electric conductor at room temperature and the resistivity increases exponentially with decreasing temperature. The resistivity of the film at 300 K was 2.5×10^{-4} Ωcm, which is lower than the bulk value (5×10^{-3} Ωcm[33]). The dlogR/dT plots (inset) show a valley at approximately 120 K. This anomaly corresponds to a Verwey transition[34], which is a type of metal–insulator transition in Fe_3O_4. The Verwey transition has been reported to sharply change the resistivity by approximately one digit[35]; however, the transition is easily disappeared by impurities or structure defects. As the Fe_3O_4 in EPI possessed magnetic and electric characteristics that were comparable to bulk Fe_3O_4, the Fe_3O_4 on γ-Al_2O_3 buffer layer was very good quality.

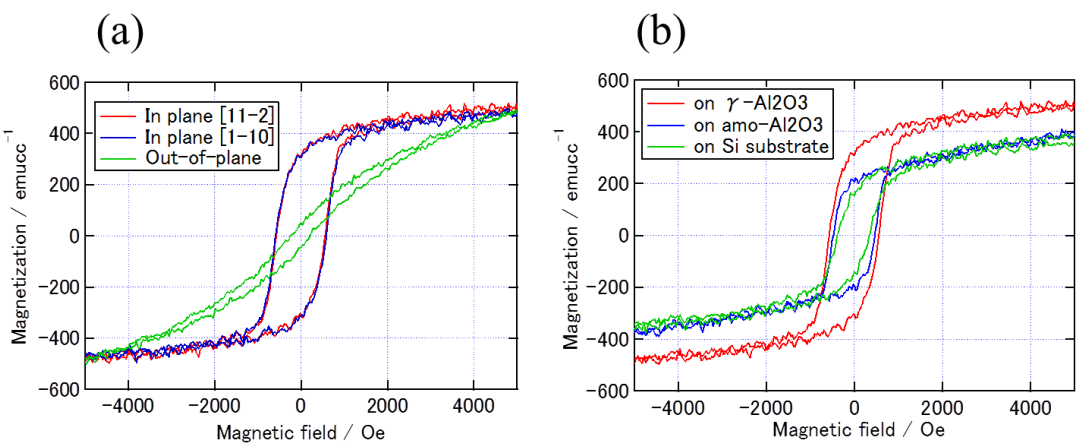

Fig. 17. (a) Magnetization curves of Fe_3O_4 on γ-Al_2O_3 in the magnetic field along [11-2], [1-10], and out of plane [111] (b) Magnetization curves of EPI, AMO, and W/O in the magnetic field along [11-2].

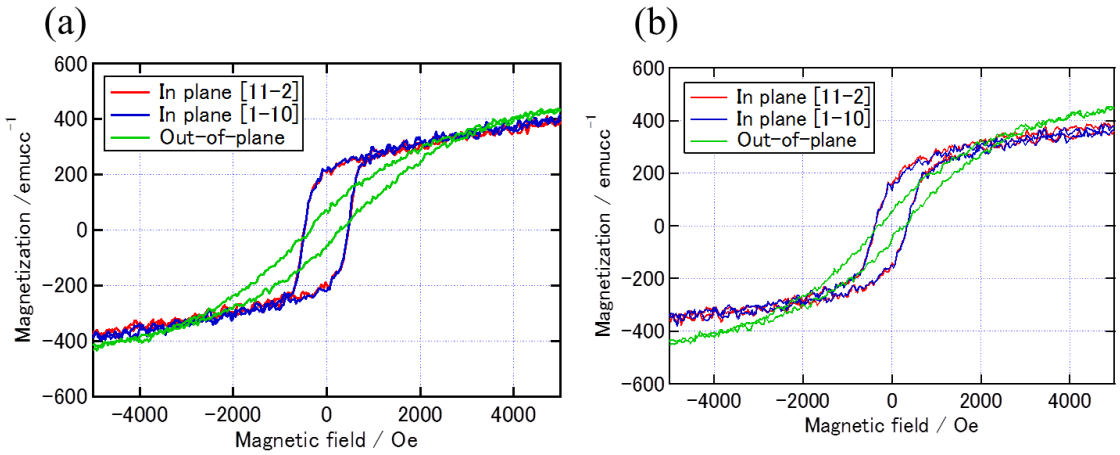

Fig. 18. Room temperature magnetization loops of (a) Fe_3O_4 on amo-Al_2O_3 and (b) Fe_3O_4 on Si substrate. The directions of the magnetic field were in-plane [11-2], in-plane [1-10] and out-of-plane [111]. Both Fe_3O_4 on the γ-Al_2O_3 buffer layer and Fe_3O_4 on the Si substrate have in-plane magnetization. The saturation magnetization (Ms) of samples (a) and (b) was approximately 400 emu/cc.

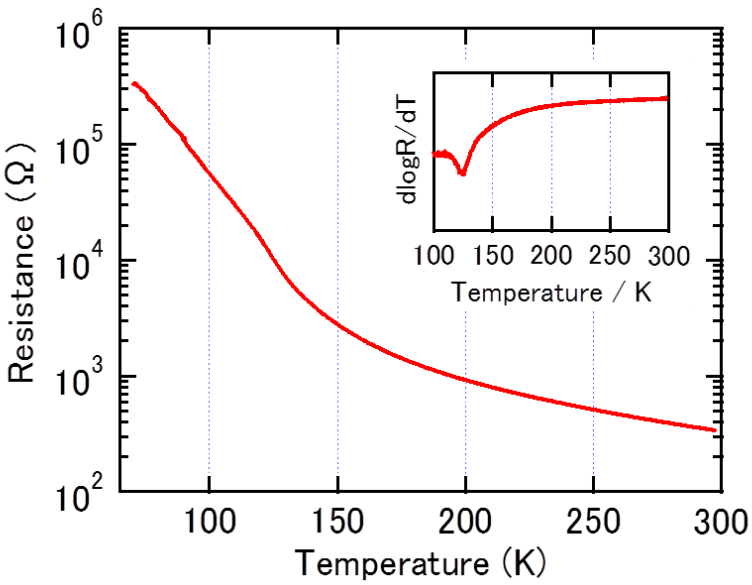

Fig. 19. The resistivity of Si(111) / γ-Al_2O_3 / Fe_3O_4 as a function of temperature. The inset is dlogR/dT plot.

2.5. Conclusions

In summary, I fabricated an epitaxial Fe_3O_4 film on a Si substrate by inserting an γ-Al_2O_3 buffer layer. From the XRD measurement and TEM observation, the γ-Al_2O_3 buffer layer contributed to the growth of epitaxial Fe_3O_4(111) on Si(111). In contrast, the Fe_3O_4 film on an amo-Al_2O_3 buffer layer had an (111)-orientation with a textured structure. The Fe_3O_4 on γ-Al_2O_3 had magnetic properties corresponding to the bulk Fe_3O_4, furthermore the resistivity exhibited a Verwey transition at 120 K. The results indicate that the heterostructure of Si substrate / γ-Al_2O_3 / Fe_3O_4 could be used as a part of magnetic tunnel junctions or spin injection devices and will allow us to integrate spintronic devices including Fe_3O_4 electrode, e.g., spin-FET or magnetic tunnel junctions, on Si.

References

[1] F. J. Jedema, H. B. Heersche, A. T. Filip, J. J. A. Baselmans, and B. J. van Wees, Nature 416, 713 (2002).

[2] O. M. J. van't Erve, A. T. Hanbicki, M. Holub, C. H. Li, C. AwoAffouda, P. E. Thompson, and B. T. Jonker, Appl. Phys. Lett. 91, 212109 (2007).

[3] S. J. Dash, S. Sharma, R. S. Patel, M. P. de Jong, and R. Jansen, Nature 462, 491 (2009).

[4] S. Datta and B. Das, Appl. Phys. Lett. 56, 665 (1990).

[5] S. Sugahara and M. Tanaka, Appl. Phys. Lett. 84, 2307 (2004).

[6] T. Sasaki, T. Oikawa, T. Suzuki, M. Shiraishi, Y. Suzuki, and K. Tagami, Appl. Phys. Exp. 2, 053003 (2009).

[7] M. Johnson and R. H. Silsbee, Phys. Rev. Lett. 55, 1790 (1985).

[8] T. Sasaki, Y. Ando, M. Kameno, T. Tahara, H. Koike, T. Oikawa, T. Suzuki and M. Shiraishi, Phys. Rev. Appied 2, 034005 (2014).

[9] M. Ohishi, M. Shiraishi, R. Nouchi, T. Nozaki, T. Shinjo and Y. Suzuki, Jpn. J. Appl. Phys. 46, No. 25, pp. L605–L607 (2007).

[10] M. Shiraishi, M. Ohishi, R. Nouchi, T. Nozaki, T. Shinjo, and Y. Suzuki, Adv. Funct. Mater. 19, 3711 (2009).

[11] M. Bibes and A. Barthélémy, IEEE Trans. Electron Devices 54, 1003 (2007).

[12] H. Yanagihara, Y. Utsumi, T. Niizeki, J. Inoue, and E. Kita, J. Appl. Phys. 115, 17A719 (2014).

[13] J. Takaobushi, T. Kanki, T. Kawai, and H. Tanaka, Appl. Phys. Lett. 98, 102506 (2011).

[14] T. Niizeki, T. Kikkawa, K. Uchida, M. Oka, K. Z. Suzuki, H. Yanagihara, E. Kita and

E. Saitoh, AIP Advances 5, 053603 (2015).

[15] A. Yanase and K. Shiratori, J. Phys. Soc. Jpn. 53, 312 (1984).

[16] A. V. Ramos, M.-J. Guittet, and J.-B. Moussy, R. Mattana, C. Deranlot, and F. Petroff, C. Gatel, Appl. Phys. Lett. 91, 122107 (2007).

[17] T. S. Santos and J. S. Moodera, Phys. Rev. B 69, 241203 (2004).

[18] Y. K. Takahashi, S. Kasai, T. Furubayashi, S. Mitani, K. Inomata, and K. Hono, Appl. Phys. Lett. 96, 072512 (2010).

[19] H. Watanabe, K. Fujita, and M. Ichikawa, Appl. Phys. Lett. 70, 1095 (1997).

[20] Yu. S. Dedkov, U. Rüdiger, and G. Güntherodt, Phys. Rev. B, 65, 064417 (2002).

[21] C. Merckling, M. El-Kazzi, G. Saint-Girons, G. Hollinger, L. Largeau, G. Patriarche, V. Favre-Nicolin, and O. Marty, J. Appl. Phys. 102, 024101 (2007).

[22] Y. C. Jung, H. Miura, and M. Ishida, Jpn. J. Appl. Phys. 38, 2333 (1999).

[23] C. Merckling, M. El-Kazzi, V. Favre-Nicolin, M. Gendry, Y. Robach, G. Grenet, and G. Hollinger, Thin Solid Films 515, 6479 (2007).

[24] W. Kern and D. Puotinen, RCA Review 31:187 (1970).

[25] S. Y. Wu, M. Hong, A. R. Kortan, J. Kwo, J. P. Man-naerts, W. C. Lee, and Y. L. Huang, Appl. Phys. Lett. 87, 091908 (2005).

[26] T. Nagahama, Y. Matsuda, K. Tate, T. Kawai, N. Takahashi, S. Hiratani, Y. Watanabe, T. Yanase, and T. Shimada, Appl. Phys. Lett. 105, 102410 (2014).

[27] L. Lari, S. Lea, C. Feeser, B. W. Wessels and V. K. Lazarov, J. Appl. Phys. 111, 07C311 (2012).

[28] A. Kawahito, T. Endo, T. Yanase, T. Nagahama, T. Shimada, J. Appl. Phys. 117, 17D506 (2015).

[29] T. Tamura, T. Yanase, T. Nagahama, M. Wakeshima, Y. Hinatsu, T. Shimada, Chem.

Lett. 43, 1569-71 (2014).

[30] C. Park, Y. Shi, Y. Peng, K. Barmark, J. G. Zhu, D. E. Laughlin, and R.M. White, IEEE Trans. Magn. 39, 2806 (2003).

[31] S. E. Shirsath, X. Liu, Y.Yasukawa, S. Li, and A. Morisako, Scientific Reports 6, 30074 (2016).

[32] R. Bachelet, P. D. Coux, B. Warot-Fonrose, V. Skumryev, G. Niu, B. Vilquin, G. Saint-Gironsb, and F. Sáncheza, Cryst. Eng. Comm., 16, 10741 (2014).

[33] W. Eerenstein, T. T. Palsra, T. Hibma, and S. Celotto, Phys. Rev. B 66, 201101(R) (2002).

[34] E. Verwey, Nature 144, 327 (1939).

[35] T. Kado, H. Saito, and K. Ando, J. Appl. Phys. 101, 09J511 (2007).

Chapter 3
Tunnel magnetoresistance of Fe_3O_4/ AlO_x/Fe on Si substrate

Fe_3O_4 with 100% spin polarization at the Fermi level is the key material for next generation spintronic devices because a high spin polarization realizes a very large magnetoresistance effect. However, epitaxial spinel ferrite films are generally grown on oxide substrates and the universal silicon substrates are rarely used due to the difficult growth condition. In this chapter, by using the Fe_3O_4 films in chapter 2, the magnetic tunnel junctions were fabricated and investigated. The negative value is expected because Fe_3O_4 has minority-spins in the Fermi level. However, the magnetoresistance effect showed 2.4%, which was considered to be due to the existence of oxygen vacancies and pinholes in the amo-Al_2O_3 barrier, and that of anti-phase boundaries in the Fe_3O_4 electrode by TEM observation.

3.1. Introduction

Magnetite with 100% spin polarization at the Fermi level is the key material for next generation spintronic devices because a high spin polarization realizes a very large magnetoresistance effect[1]. The conventional magnetic tunnel junctions using epitaxial Fe_3O_4 have been fabricated on MgO substrates[2,3]. Meanwhile, magnetic tunnel junctions using epitaxial Fe_3O_4 on Si substrate which is the most universal substrate are rarely reported, and the conduction behavior has not been clarified[4]. In order to diffuse the spintronics devices widely, combination with Silicon technology is inevitable. In this chapter, I investigated the growth conditions of Fe_3O_4 and fabricated magnetic tunnel junctions using Fe_3O_4 as an electrode. In addition, I investigated its magneto-transport properties and the interface state between Fe_3O_4 and tunnel barrier. Adding to that the observation of Fe_3O_4 grain boundary was carried out using a transmission electron microscope in order to evaluate the validity of the magnetoresistance effect.

3.1.1. Tunnel Magnetoresistance (TMR)

The TMR effect has been discovered before the GMR effect was discovered. In 1975, Jullière demonstrated the TMR effect in Co / Ge / Fe junctions[5]. Then, in 1982, Maekawa and Gäfvert reported the TMR effect which is shown in Ni/NiO/Ni junctions[6]. The Ge layer was a semiconductor, and the NiO layer was an insulator. After that, Miyazaki et al. demonstrated the TMR effect of 20% in Fe / Al-O / Fe junctions in 1995[7]. Later, many researchers have studied the TMR effect in magnetic tunnel junctions.

Jullière model that is a simple theory model of TMR mechanism propounded by Jullière is shown in Fig. 1. First, it is assumed that the spins of electrons are fixed during the tunneling. When the magnetization configurations of two magnetic metal layer are

parallel, the major spins in Fermi level are tunneling into majority spins states ($D_{1\downarrow} \rightarrow D_{2\downarrow}$). On the other hand, when the magnetization configurations of the electrodes are antiparallel, the major spins in Fermi level are tunneling to minority spin states ($D_{1\downarrow} \rightarrow D_{2\uparrow}$). Therefore, the tunnel current in parallel configuration is larger than that of antiparallel. The tunnel magnetoresistance ratio (TMR ratio) which is the rate of change of tunnel resistance, was defined as follows:

$$\text{TMR ratio (\%)} = \frac{R_{Ap} - R_p}{R_p} \times 100$$

Where, the R_{ap} is the resistance of antiparallel magnetic configuration. The R_p is the resistance of parallel configuration. Since the R_{ap} is usually larger than R_p, it is possible the TMR ratio to be infinite when R_{AP} is infinite, namely insulating.

Then, the spin polarization (P) of magnetic metal is given by:

$$P_{\xi} = \frac{D_{\xi,\uparrow}(E_F) - D_{\xi,\downarrow}(E_F)}{D_{\xi,\uparrow}(E_F) + D_{\xi,\downarrow}(E_F)} \qquad \xi = 1,2$$

Where, ξ is the layer number of magnetic electrode, the $D_{\xi,\uparrow}(E_F)$ and $D_{\xi,\downarrow}(E_F)$ are the density of states of majority and minority spin in Fermi level, respectively. The P of nonmagnetic material is zero.

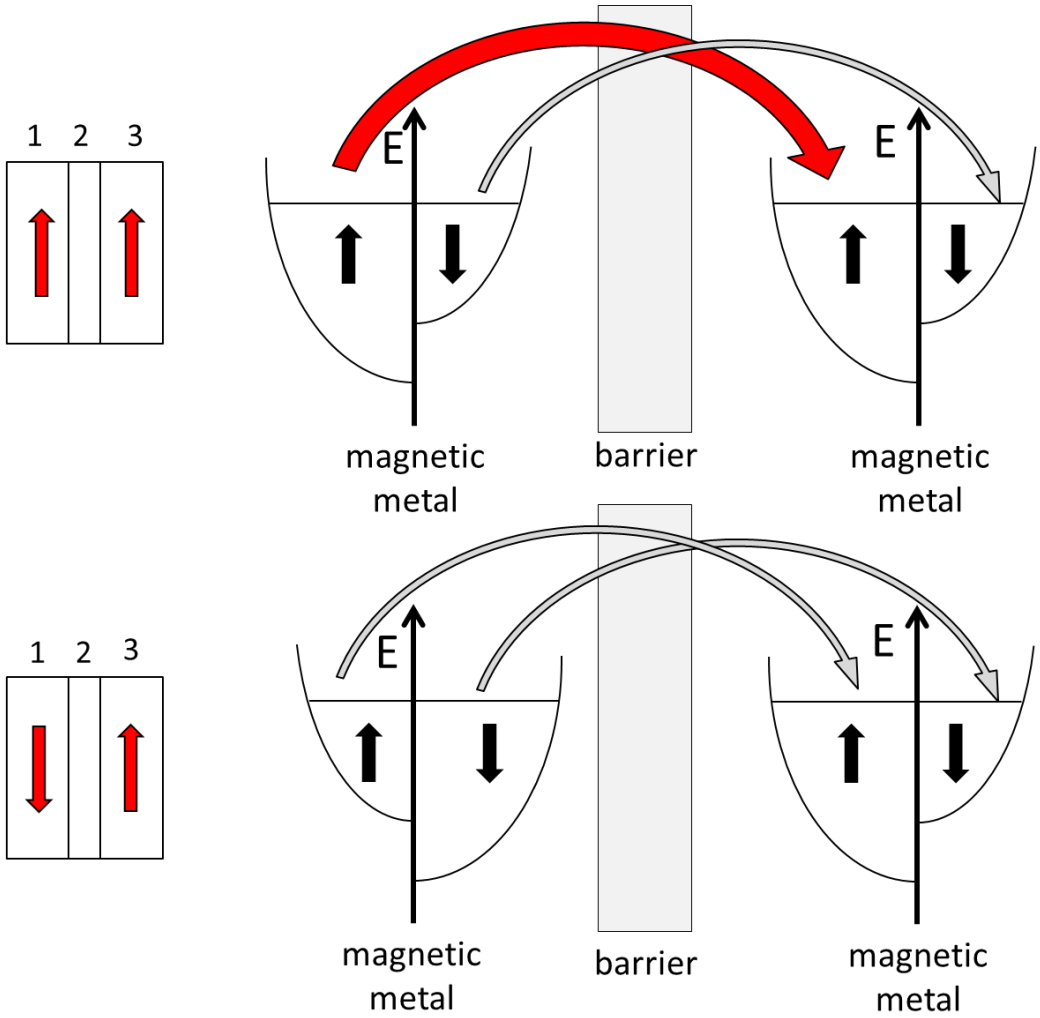

Fig. 1. Mechanism of magnetic tunnel junctions

Using P, the TMR ratio is also expressed by:

$$\text{TMR ratio (\%)} = \frac{2P_1P_2}{1 - P_1P_2} \times 100$$

If we know P of a ferromagnetic layer, we can calculate the spin polarization of another electrode.

The schematic image of a typical result of TMR effect is shown in Fig. 2. The measurement is started under large negative magnetic field (left hand side). When the magnetic filed (H) detrcease to zero, the tunnel resistance independent with H. Then,

positive H is applied. At the coercive filed of one electrode, the resistance increases because the magnetization of a ferromagnetic metal flipped and antiparallel magnetic configuration is realized. In addition, by applying the magnetic field more, the magnetization of another electrode is reversed, that the resistance decreases due to parallel magnetic configuration. By sweeping the magnetic field from this state to negative magnetic field, same process takes place.

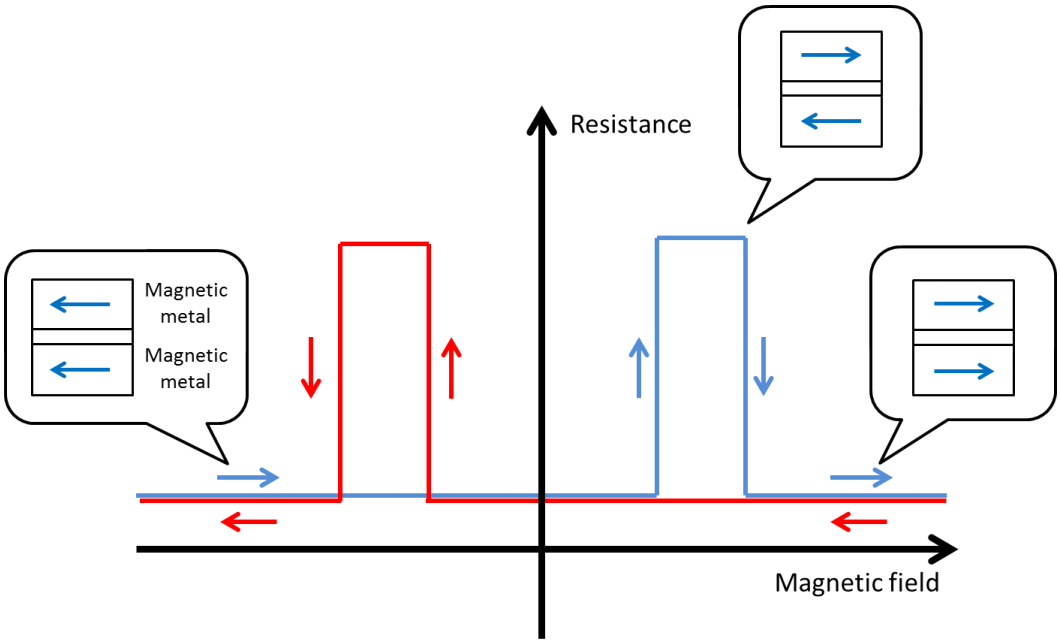

Fig. 2. Schematic image of TMR curve.

At the beginning of the TMR development, the Al_2O_3 has been widely used as a tunnel barrier, and the TMR ratio of the magnetic tunnel junction was improved year by year. However, the value of TMR ratio was about 50% even after 2000. For further improvement of TMR ratio, Mathon et al.[8] and Butler et al.[9] conducted the first principle calculation of the TMR ratio of magnetic tunnel junctions (MTJs) with single crystal MgO barrier. The calculation presented the possibility of the TMR ratio of 1000%. The result encouraged many researchers to fabricate the MTJs with single crystal MgO-

tunnel barrier. Finally, In 2004, the Yuasa et al.[10] and Parkin et al.[11] reported the TMR ratio of up to 200% in Fe / MgO / Fe MTJs at room temperature. After that, the magnetic metals for the electrodes were improved by FeCoB or Heusler alloy, which caused the TMR ratio to be 500% (1000%) at room (law) temperature.

3.2. Experimental Section

3.2.1. Experimental Method

The layer structure for of the MTJs were Si(111) / γ-Al_2O_3 / Fe_3O_4 / amo-Al_2O_3 / Fe / Co / Au . The Fe_3O_4 and Fe/Co layer were ferromagnetic electrode and amo-Al_2O_3 was the tunnel barrier. Firstly, I confirmed the crystallizations and flatness of the bottom electrodes, Fe_3O_4 because the bottom electrodes should have the flat surface to obtain a homogeneous tunnel barrier, and good crystallinity is necessary for appropriate magnetic properties. Then, the MTJs were fabricated and the magneto-transport properties were investigated.

Before deposition, the Si substrate was treated by the RCA method and HF solution and annealed at 900°C under a vacuum of <10^{-6} Pa. The γ-Al_2O_3 buffer layer was formed by evaporating the Al_2O_3 source material at 900°C and annealing at 900°C for 30 minutes. In previous reports, γ-Al_2O_3 was grown at >850°C and under a vacuum of <10^{-6} Pa[12], and the growth conditions I used for γ-Al_2O_3 were in the range of the report. In Si(111) / γ-Al_2O_3 / Fe_3O_4 / amo-Al_2O_3, which was fabricated to see the crystallization and flatness of the Fe_3O_4, the Fe_3O_4 film was formed by reactive deposition at 300-450°C or deposition rate of 0.1-0.45 Å/s under a O_2 atmosphere of 4.0×10^{-4} Pa. The samples were fabricated under various growth conditions, i.e. annealing temperature, substrate temperature and deposition rate. The quality of the Fe_3O_4 strongly depended on them. The amo-Al_2O_3 was

grown at room temperature in a vacuum of <4×10^{-4} Pa and annealed at 150°C for 30 minutes. The epitaxial growth and crystal structure were confirmed by TEM. The cross-sectional samples for TEM were prepared by using conventional mechanical polishing and dimpling techniques.

To investigate magneto-transport, we fabricated the films on the Fe_3O_4 film. The sample structure was Si(111) / γ-Al_2O_3 / Fe_3O_4 / amo-Al_2O_3 / Fe / Co / Au as shown in Fig. 3. Because the current in MTJs flowed perpendicular to the plane, the multilayer should be fabricated into the devices by using the microfabrication process. The I-V characteristics and magnetoresistance effect was measured by DC measurements.

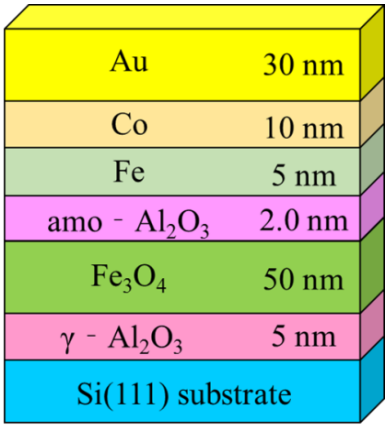

Fig.3. Sample structure

3.2.2. Microfabrication Techniques

To measure the electrical properties, the samples were processed into devices by using some equipment. The preparation steps are shown for microfabrication process in Fig.4, and described successively.

1. The specimen surface is carefully cleaned with N_2 blow in order to obtain perfectly clean surfaces.
2. The light-sensitive film is applied to the surface of substrate with spincoater. PMGI

and OFPR800LB are used as the light-sensitive film.

3. The light-sensitive films are exposed by ultraviolet for 9 ~ 12 sec.
4. The light-sensitive films are developed by dipping the NMD-3 (developer) and water (rinse).
5. The sample enters the milling chamber and mill the
6. The SiO_2 is deposited by the spattering. The thickness of SiO_2 layer is 100 nm.
7. The remaining light-sensitive films are removed by dipping the 1-methyl-2-pyrrolidone (remover) and water (rinse).
8. Same as 2.
9. Same as 3.
10. Same as 4.
11. Cr and Au films are deposited by spattering system or vacuum deposition.
12. Same as 7.

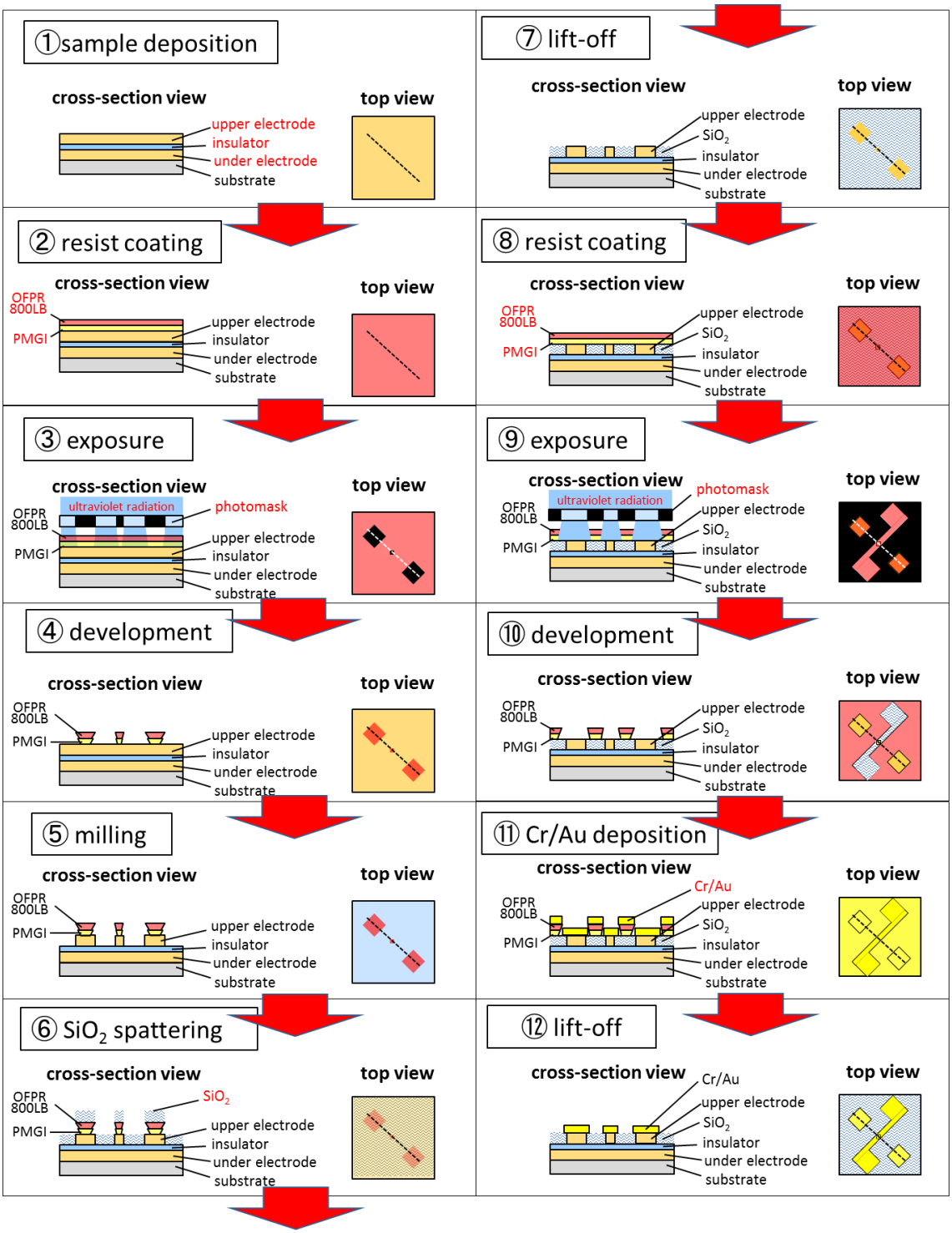

Fig. 4. Microfabrication process

3.2.3. Estimation of Barrier Height

In order to assess the tunnel barrier of magnetic tunnel junctions, the barrier height and the width of thickness are estimated by electrical properties. Fig. 5 is the graph which is the resistance area (RA) at T = 20 K (measured at a bias voltage of 10 mV) versus the thickness of tunnel barrier[1]. The scale of Vertical axis is logarithm.

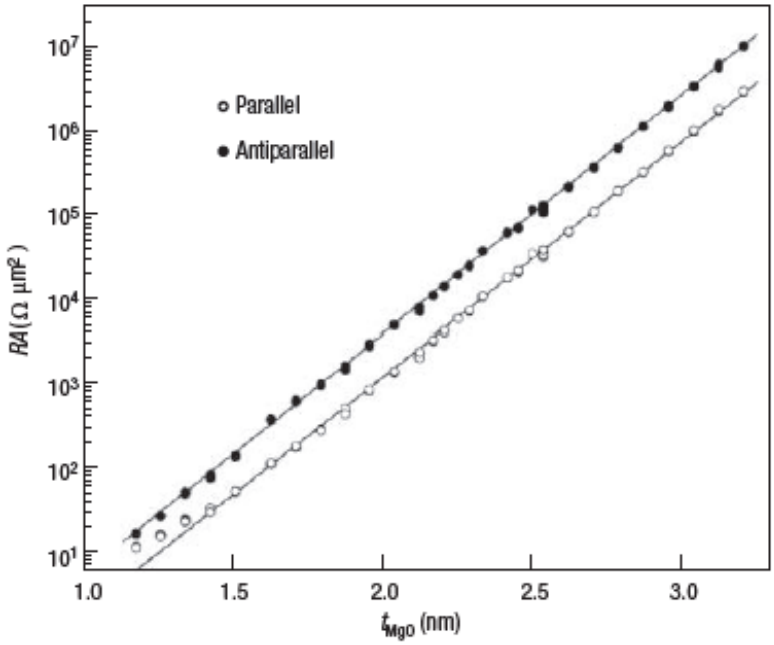

Fig.5. The resistance area versus thickness of tunnel barrier[10]

According to the Wenzel–Kramer–Brillouin (WKB) approximation[13], the slope of the log(RA) versus thickness of tunnel barrier is shown in the following equation.

$$\text{The slope of log(RA) versus thickness of tunnel barrier} = -\frac{4\pi\sqrt{2m\phi}}{h}$$

where m is the electron mass, ϕ is the potential barrier height (energy difference between the Fermi level and the bottom of the conduction band in the tunnel barrier) and h is the Planck's constant. S. Yuasa et al, reported that the slope yields a barrier height ϕ of 0.39 eV[10].

3.2.4. Estimation of barrier height by Simmons Fitting

Another way to estimate the barrier height is Simmons fitting, which is reported by Simmons in 1963[13]. Simmons' equation is assumed to be the case where the Fermi levels of the two electrodes are the same height.

The formula is as follows.

$$J = \left(\frac{e}{2\pi h s^2}\right)\left\{\left(\phi_0 - \frac{eV}{2}\right) exp\left[-\frac{4\pi s}{h}(2m)^{\frac{1}{2}}\left(\phi_0 - \frac{eV}{2}\right)^{\frac{1}{2}}\right]\right.$$
$$\left. -\left(\phi_0 + \frac{eV}{2}\right) exp\left[-\frac{4\pi s}{h}(2m)^{1/2}\left(\phi_0 + \frac{eV}{2}\right)^{1/2}\right]\right.$$

where J is the the density of electrons, m is the electron mass, s is the thickness of barrier, ϕ_0 is the barrier height, V is the voltage. This equation shows the approximate electron transport when there is no difference in potential between up-spin and down-spin. In addition, this equation is generally corresponded to the electron transport with the Al_2O_3 barrier. In the case of MgO barrier, Simmons' equations for I–V characteristics yield ϕ = 0.37–0.40 eV[10]. The barrier height is considerably lower than the values in the literature. However, it should be noted that it is not corresponded to be the electron transport with the MgO barrier because the electrical transport property is the coherent tunneling in the MgO barrier.

3.3. Results and Discussion

3.3.1. Crystallization and flatness by RHEED and AFM

As shown in chapter 2, the γ-Al_2O_3 buffer layer makes the Fe_3O_4 layer on Si substrate more epitaxial. The qualities of fabricated films usually depend on deposition rate, annealing, substrate temperature during deposition and so on. Fig. 6 shows the RHEED patterns of Fe_3O_4 film fabricated under the various conditions. The direction of the incident electron beam was [11-2]. Fig. 6 (a) shows the RHEED pattern of the Fe_3O_4 films fabricated at the deposition rate of 0.1 Å/s and at the substrate temperature of 300℃. The RHEED pattern was clear streak pattern and the half streak pattern was observed, which indicated that the Fe_3O_4 film grew epitaxially and there was surface reconstruction called p(1x1) structure. Fig. 6 (b) shows the RHEED pattern of the Fe_3O_4 films which was fabricated at same condition of Fig. 6 (a) and annealed at 600°C. The RHEED pattern was clear streak pattern. However, the half streak pattern was not observed after the annealing, which indicated that the Fe_3O_4 film have no surface reconstruction. Fig. 6 (c) shows the RHEED pattern of the Fe_3O_4 films fabricated at the deposition rate of 0.1 Å/s and at the substrate temperature of 450°C. The RHEED pattern was spot and streak pattern. The half streak pattern was spotty and streak, which indicated that the Fe_3O_4 film had a rough surface. Fig. 6 (d) shows the RHEED pattern of the Fe_3O_4 films fabricated at the deposition rate of 0.45 Å/s and at the substrate temperature of 300°C. The RHEED pattern was rather spotty and including ring pattern, which indicated that the surface was rough and film included polycrystalline grains.

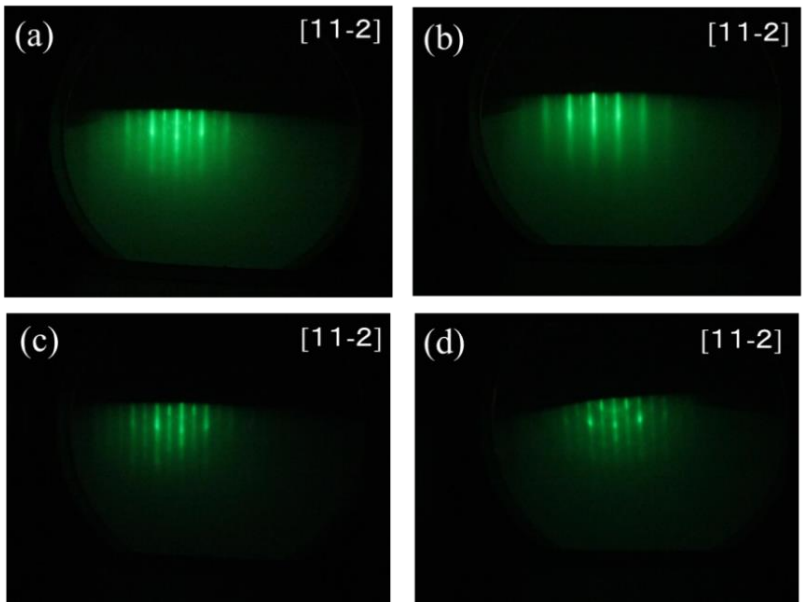

Fig. 6. RHEED pattern of Fe_3O_4 (a) deposition rate of 0.1 Å/s and substrate temperature of 300°C (b) after annealed at 600°C, (c) deposition rate of 0.1 Å/s and substrate temperature of 450°C (d) deposition rate of 0.45 Å/s and substrate temperature of 300°C

In order to show the relationship with the deposition rate, Fig. 7 shows in detail that the RHEED patterns and AFM images of the Fe_3O_4 fabricated at different deposition rate. Fig. 7 (a) - (c) showed the RHEED patterns of Fe_3O_4 fabricated at deposition rate of 0.1 Å/s, 0.3 Å/s and 0.45 Å/s respectively. The direction of the incident electron beam was [11-2]. The RHEED pattern of Fig. 7 (a) was streak pattern, and that of Fig. 7 (b) was ring and streak pattern indicating that the Fe_3O_4 slightly has polycrystalline. In Fig. 7 (c), the RHEED pattern turned into ring pattern indicating that large part of Fe_3O_4 film has polycrystalline surface.

Fig. 7 (d)-(f) show the AFM images of the Fe_3O_4 deposited at different Temperature: 0.1 Å/s, 0.3 Å/s and 0.45 Å/s. In Fig. 7 (d)-(f), the values of the roughness average, Ra, were 0.35 nm, 0.85 nm and 1.13 nm. Depending on the deposition rate, the roughness average

increased and the size of crystal grains became smaller. Such deposition rate dependence could be attributed with the balance between the diffusion speed on the surface and material supply.

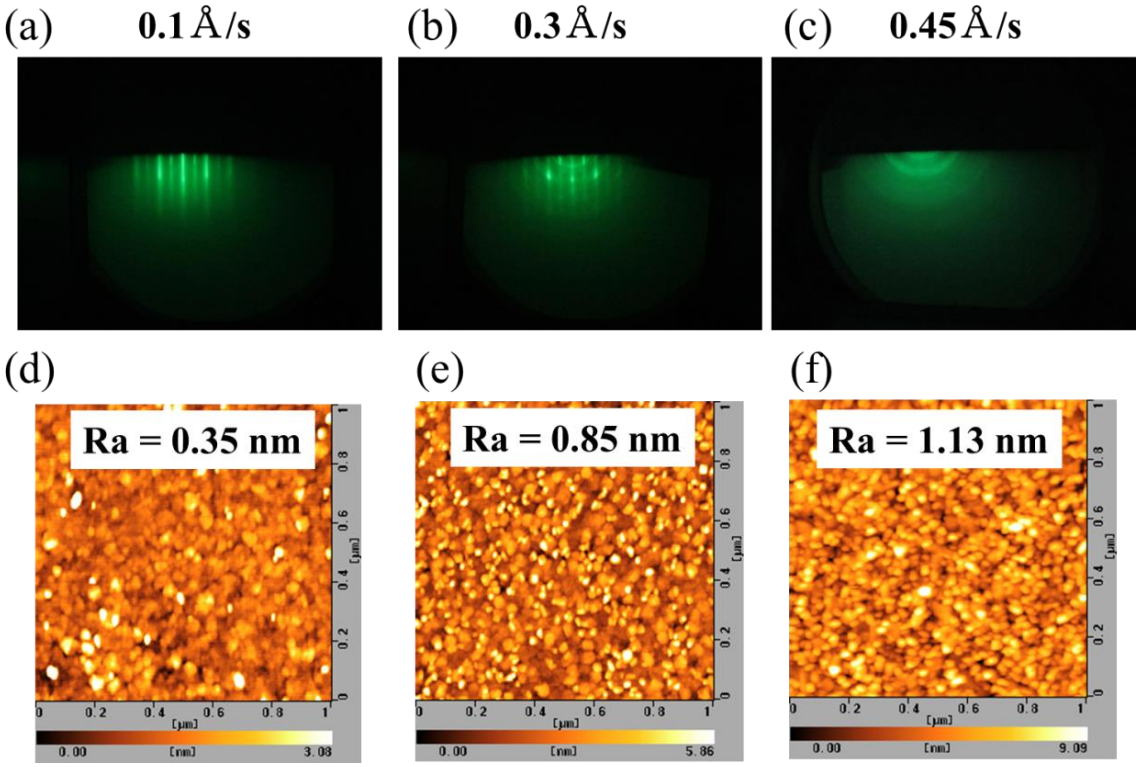

Fig. 7. RHEED patterns and AFM images of Fe_3O_4 fabricated at deposition rate of (a) (d) 0.1 Å/s, (b) (e) 0.3 Å/s and (c) (f) 0.45 Å/s

3.3.2. Anti-phase Boundary in Fe_3O_4 Film

The Fig.8 (a) and (b) shows the cross-sectional TEM images of Si(111)/ γ-Al_2O_3 2.4 nm / Fe_3O_4 30 nm / amo-Al_2O_3 2 nm. The incident direction of electrons was [1-10]. Flat layers were observed in the range of tens of nanometers as shown in Fig. 8 (a). It can be seen that the atomic layers in the Fe_3O_4 film are aligned in the direction parallel to the substrate. In Fig. 8 (b), the atomic layers were also observed clearly, and there was a

boundary in the vertical direction of the image, in which the atomic layers were misaligned between the left and right sides of the boundary. It indicated that the Fe_3O_4 layer contains the antiphase-boundary (APB) which is usually shown in epitaxial Fe_3O_4 films grown on MgO substrate[14,15]. In the layer with the APB, each domain has anti-parallel magnetic arrangement due to antiferromagnetic coupling at APB, which causes the imperfect parallel magnetic configuration. That could suppress the TMR effect in the MTJ.

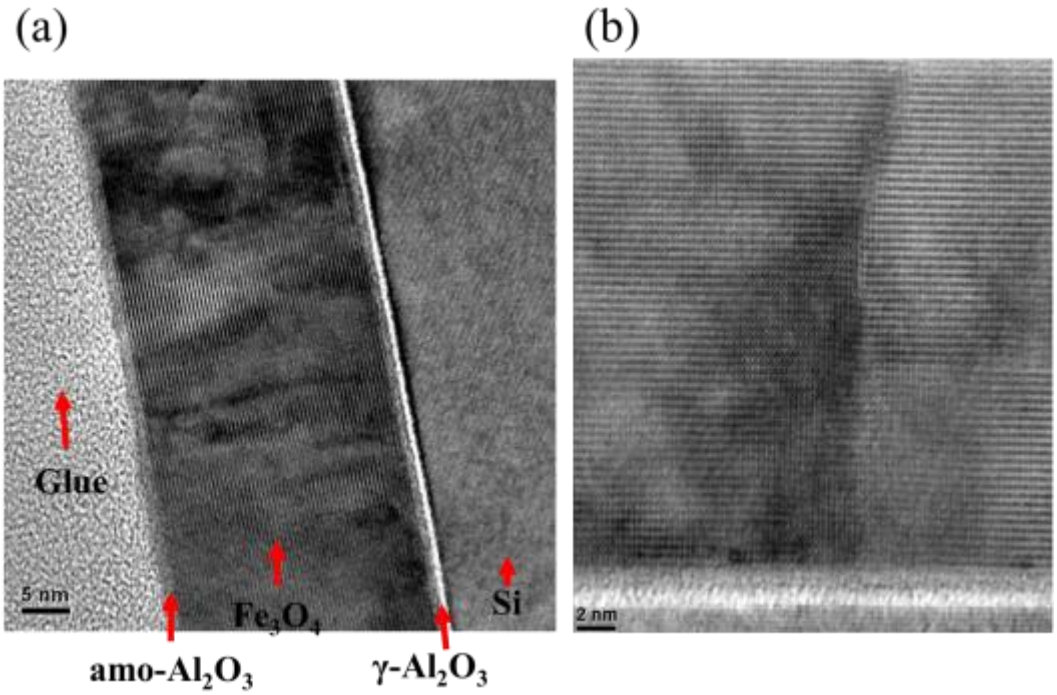

Fig. 8. Cross-section TEM image of (a) low magnification (b) high magnification

3.3.3. Magnetoresistance and Electrical Properties of Fe_3O_4

I fabricated the MTJs of Fe_3O_4 / Al_2O_3 / Fe and measured the TMR ratio and the I-V characteristics in zero magnetic fields, as shown in Fig. 9. The size of the junction was 10×10 μm^2 and the thickness of Al_2O_3 barrier was 2.0 nm. The MR ratio of 2.4 % at 10

mV was observed as shown in Fig. 9 (a) (red line). The magnetic field was applied at the direction of [1-10]. The shape of the MR curve was different from that of anisotropic magnetoresistance (AMR)[16], which is the magnetoresistance measured in a single film. Therefore the TMR effect was responsible for the in Fig. 9 (a), although the sign of the MR was plus, that is opposite to the theoretical prediction.

The Nonlinear I–V characteristic at 150 K was also observed as shown in Fig. 9 (b), which means that the electrical transport was tunneling. By using the Simmon's formula fitting, the barrier height was not able to be estimated, though the barrier height of conventional Fe_3O_4 / Al_2O_3 / Fe systems was estimated as 0.9 eV in the previous paper[17]. The results indicated that the Al_2O_3 layer in MTJs on Si substrate was leaky due to the hopping site in the barrier or pinholes.

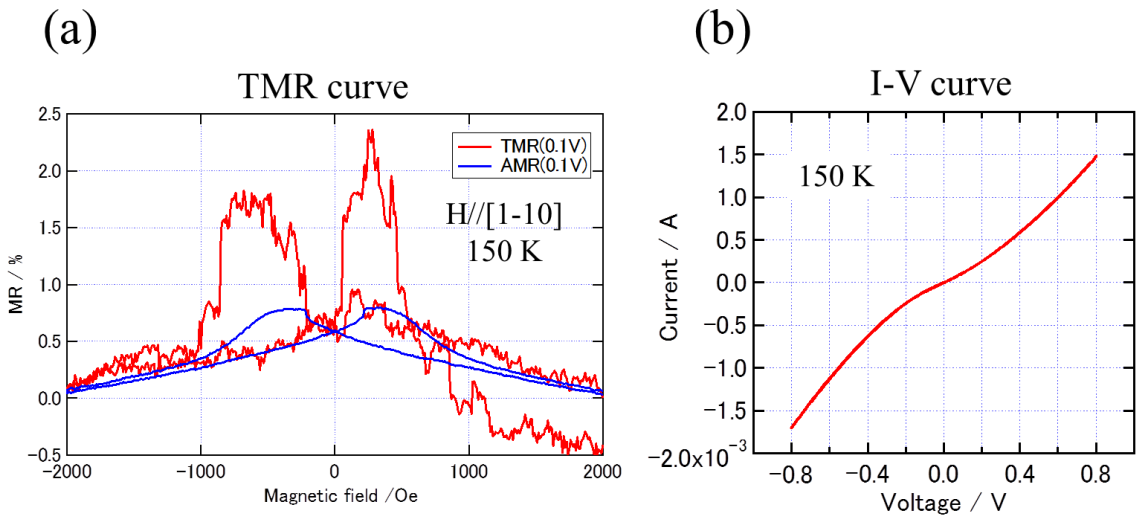

Fig. 9. (a) Magnetoresistance curve and anisotropic magnetoresistance curve and (b) I–V characteristics at 150 K with a bias voltage of 10 mV

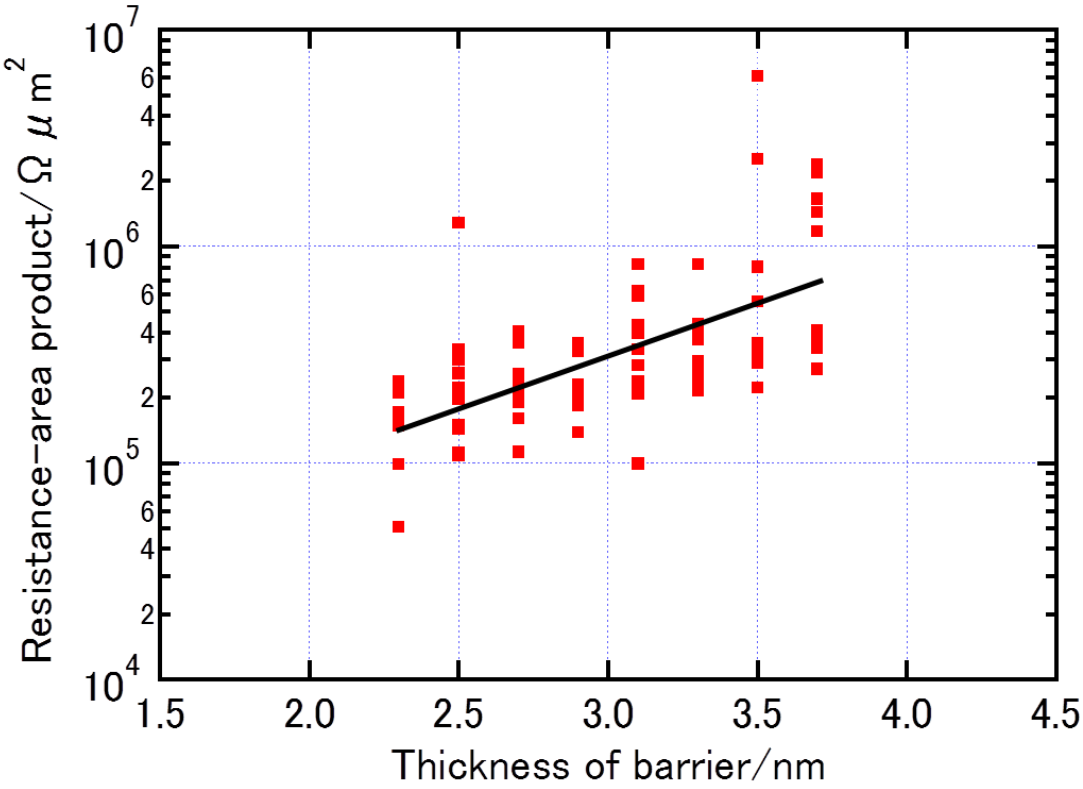

Fig. 10. Resistance area products at 150 K measured at a bias voltage of 10 mV versus thickness of Al_2O_3 barrier

The resistance area products (RA) of the MTJs were plotted as a function of the thickness of Al_2O_3 barrier in Fig. 10. The exponential increase depending on the thickness of barrier is typical behavior of ideal tunnel junctions[10]. The slope of the log(RA) versus thickness of barrier corresponds to $4\pi(2m\phi)^{1/2}/h$, where m is the electron mass, ϕ is the potential barrier height, and h is the Planck's constant. The slope provided a barrier height ϕ of 0.013 eV, which is smaller than conventional barrier height of Al_2O_3. It was suggested that the oxygen vacancies and pinholes existed in the barrier.

3.4. Conclusions

I fabricated the magnetic tunnel junctions of the Fe_3O_4 / Al_2O_3 / Fe on Si(111) substrate and investigated their epitaxial growth and magneto-transport properties. By reducing the film forming rate, the crystallinity and flatness of Fe_3O_4 were improved very much. With regard to the magneto-transport, the TMR ratio of 2.4% was obtained, which is reverse to the theoretical prediction and obtained experimentally in previous papers. Such TMR effects could be attributed to the existence of anti-phase boundaries in the Fe_3O_4 electrodes and the hopping site due to oxide ion vacancies and pinholes in the amo-Al_2O_3 barrier.

References

[1] I. Leonov, A. N. Yaresko, V. N. Antonov, V. I. Anisimov, Phys. Rev. B. 74, 165117 (2006).

[2] T. Nagahama, Y. Matsuda, K. Tate, S. Hiratani, Y. Watanabe, T. Kawai, N. Takahashi, T. Yanase, T. Shimada, Appl. Phys. Lett. 105, 102410 (2014).

[3] F. Greullet, E. Snoeck, C. Tiusan, M. Hehn, D. Lacour, O. Lenoble, C. Magen, and L. Calmels, Appl. Phys. Lett 92, 053508 (2008).

[4] C. Park, J. G. Zhu, Y. G. Peng, D. E. Laughlin, and R. M. White, IEEE Trans. Magn. 41, 2691 (2005); C. Park, Y. Shi, Y. Peng, K. Barmak, J. G. Zhu, D. E. Laughlin, and R. M. White, IEEE Trans. Magn. 39, 2806 (2003).

[5] M. Julliere: *Phys. Lett.* **54A**, 225 (1975).

[6] S. Maekawa, U. Gafvert, IEEE Trans. Magn., 18, 707 (1982).

[7] T. Miyazaki and N. Tezuka, J. Magn. Magn. Mater. 98, L7 (2005). ; J. S. Moodera, L. R. Kinder, T. M. Wong and R. Meservey, Phys. Rev. Lett. 74, 3273 (1995).

[8] J. Mathon and A. Umerski, Phys. Rev. B 63, 220403(R), (2004).

[9] W. H. Butler, X. –G. Zhang, T. C. Schulthess, and J. M. MacLaren, Phys. Rev. B 63, 054416 (2001).

[10] S. Yuasa, T. Nagahama, A. Fukushima, Y. Suzuki, K. Ando, Nature Mater. 3, 868 (2004)

[11] S. S. P. Parkin, C. Kaiser, A. Panchula, P. M. Rice, B. Hughes, M. Samant, S. Yang: *Nature Mater.* **3**, 862 (2004).

[12] C. Merckling, M. El-Kazzi, V. Favre-Nicolin, M. Gendry, Y. Robach, G. Grenet, and G. Hollinger, Thin Solid Films 515, 6479 (2007).

[13] J. G. Simmons, J. Appl. Phys. **34**, 1793 (1963).

[14] J. F. Bobo, D. Basso, E. Snoeck, C. Gatel, D. Hrabovsky, J. L. Gauffier, L. Ressier, R.

Mamy, S. Visnovsky, J. Hamrle, J. Teillet, and A. R. Fert, Eur. Phys. J. B 24, 43-49 (2001).

[15] A. Ikeuchi, S. Hiura, T. Mizuno, E. Kaji, A. Subagyo and K. Sueoka, Jpn. J. Appl. Phys. 51, 08KB02, (2012).

[16] K. Matsuzaki, V. K. Lazarov, L. Lari, H. Hosono, and T. Susaki, Journal of Physics D, 46(2), 022001 (2012).

[17] K. S. Yoon, J. H. Koo, Y. H. Do, K. W. Kim, C. O. Kim, J. P. Hong, J. Magn. Magn. Mater. 285, 125 (2005).

Chapter 4
Investigation of epitaxial growth and tunnel magnetoresistance effects in magnetic tunnel junctions including spinel ferrite layers

The combination of magnetic tunnel junctions (MTJs) and magnetic insulating (MI) layers has attracted much attention because of its potential for use in novel spintronic devices. To realize such devices, the epitaxial growth and magnetoresistance of MTJs with spinel ferrite were investigated. Non-magnetic (NM) layers were inserted between the MTJs and MI layers as magnetic decoupling layers, the epitaxial growth of which was important to obtain high-quality epitaxial multilayers. A multilayer of MTJ/NM/MI and MI/NM/MTJ was fabricated and tunnel magnetoresistance (TMR) values of 70% and 50% at room temperature, respectively, were observed. The shape of the magnetoresistance curve depended on the sample structure.

4.1. Introduction

In spintronics research, the epitaxial multilayer technique is an important technology. A fully epitaxial junction of Fe/MgO/Fe enabled the development of a new class of spintronic devices such as magnetoresistive random access memory (MRAM) devices[1][2]. Recently, novel spintronic phenomena in magnetic insulators (MIs) have attracted much attention because of their potential to be used to create post-MRAM devices. Uchida et al. demonstrated that yttrium iron garnet (YIG) films, which are typical MIs, transferred the electric signals by a spin current generated by spin waves[3]. Other researchers are developing the spin-wave control in YIG for logic devices, which is called magnonics[4]. Furthermore, Slonczewski proposed the enhancement of the spin-torque transfer in magnetic tunnel junctions (MTJs) by the spin current generated by the spin wave in MIs[5]. The MI films also have a function of filtering the spin in the tunneling process, so that they have been investigated as spin-filter tunnel barriers[6].

To realize such new functional devices, the film-growth technique of MgO–MTJs with the MI is crucial because the MTJs and MI should be integrated on the same substrates. Although YIG is the most popular MI material in spin-current research, YIG epitaxial films are generally grown only on gadolinium gallium garnet (GGG) substrates. Fabrication of functional devices is slightly difficult as magnetic metallic layers or metallic electrodes must be inserted between the substrates and MI layers in the devices. Spinel ferrites, e.g., Fe_3O_4 or $CoFe_2O_4$, are promising candidates for the MI in such complex devices because of the epitaxial growth on some metallic layers and a high Curie temperature[7]. Since the fabrication of MgO–MTJs and magnetic-oxide films has been developed independently thus far, their combination has not yet been established. In this study, I investigated the epitaxial growth of multilayers comprising magnetic oxide and

MgO–MTJs and measured the magnetoresistance effect. I succeeded in fabricating the junctions and observed a tunnel magnetoresistance (TMR) effect of 70% at room temperature.

4.2. Experimental Section

To grow all the layers epitaxially, I selected the spinel ferrites $CoFe_2O_4$ and Fe_3O_4 as the magnetic-oxide layer. The lattice constant of the spinel ferrites is approximately 0.84 nm, which is twice that of MgO (0.42 nm)[8]. The small lattice mismatch is favorable for the epitaxial growth, which is important to achieve a large TMR ratio in MgO–MTJs and good magnetic properties of the ferrites.

The two sample structures that I fabricated were

(1) MgO(001) substrate/MgO 20 nm/Fe 50 nm/MgO 2 nm/CoFe 5 nm/non-magnetic layer (NM) (Au, Cr, Pt) 3 nm/$CoFe_2O_4$ 5 nm/Cr 10 nm/Au 30 nm and

(2) MgO(001) substrate/MgO 20 nm/TiN 50 nm/Fe_3O_4 50 nm/Cr 5 nm/Fe 3 nm/MgO 1.5 nm/Fe 50 nm/Cr 10 nm/Au 30 nm.

For sample (1) shown in Fig. 1(a), the $CoFe_2O_4$ layer was grown on the MTJs (Fe/MgO/Fe) separated by an NM layer. The NM layer magnetically decoupled the thin Fe and $CoFe_2O_4$ layer, enabling us to control the magnetization of Fe and $CoFe_2O_4$ independently. I employed three metals, Cr, Au, and Pt as the NM layer to investigate the epitaxial growth of the $CoFe_2O_4$ layer on the NM layer. The $CoFe_2O_4$ layer should be very thin because the current must flow across the layer for TMR measurements (Fig. 1). With respect to the magnetic properties, such thin spinel ferrite films exhibit low squareness of hysteresis because of the anti-phase boundary[9][11].

To obtain high squareness of the magnetic hysteresis of the spinel ferrites, I designed

sample (2) to have a thick Fe_3O_4 layer under the MTJs as shown in Fig. 1(b). The current can flow in the Fe_3O_4 layer because of its electrical conductivity, even though the resistance is 100-fold larger than that of conventional metals[12][13]. For sample (2), Cr was used as the NM layer because of the epitaxial growth of Cr on Fe_3O_4(001).

The multilayers were prepared on an MgO(001) substrate using molecular beam epitaxy (MBE). An MgO buffer layer with a thickness of 20 nm was grown in a vacuum at 1.0×10^{-7} Pa at 400°C on an MgO(100) substrate prebaked at 800°C. For sample (1), the MgO–MTJ was deposited on the MgO buffer layer, the growth conditions of which are described elsewhere[1][14]. I used two fabrication methods for $CoFe_2O_4$: thermal oxidation and reactive deposition. The thermal oxidation[15] involved oxidation in an oxygen radical of 4.0×10^{-4} Pa at 300°C, which followed Fe and Co deposition. The reactive deposition[16] involved deposition in an oxygen radical atmosphere. After the $CoFe_2O_4$ deposition, the films were annealed at 300°C for 30 min.

For sample (2), a TiN layer was deposited in N_2 atmosphere on the MgO buffer followed by the growth of Fe_3O_4 layer in an O_2 atmosphere at 4.0×10^{-4} Pa at 300°C. The MgO–MTJs were fabricated under the same conditions as in sample (1). Tunnel junctions were prepared using standard microfabrication techniques (e.g., photolithography, electron beam lithography, Ar-ion milling, and SiO_2 sputtering). The epitaxial growth was examined using reflection high-energy electron diffraction (RHEED), and the surface morphology was examined using atomic force microscopy (AFM). I also investigated the I–V characteristics and TMR effect using DC measurements.

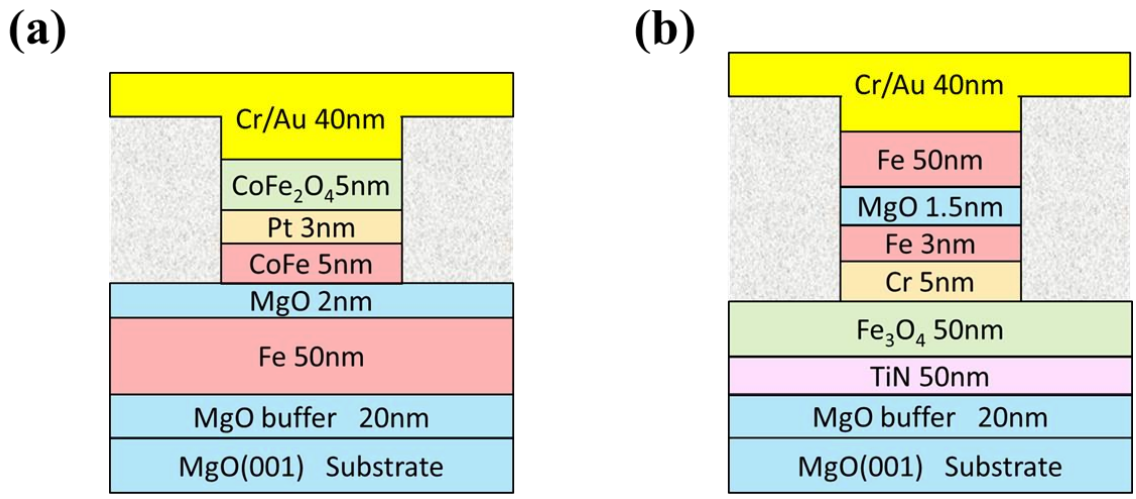

Fig. 1. Schematic of the MgO–MTJs with spinel ferrite layers: (a) MgO(001) substrate/MgO 20 nm/Fe 50 nm/MgO 2 nm/CoFe 5 nm/(Au, Cr, Pt) 3 nm/$CoFe_2O_4$ 5 nm/Cr 10 nm/Au 30 nm and (b) MgO(001) substrate/MgO 20 nm/TiN 50 nm/Fe_3O_4 50 nm/Cr 5 nm/Fe 3 nm/MgO 1.5 nm/Fe 50 nm/Cr 10 nm/Au 30 nm.

4.3. Results and Discussion

4.3.1. Crystallization and Flatness of Ferrite Layers by RHEED and AFM

In sample (1), the $CoFe_2O_4$ layer was needed to be grown epitaxially on the NM decoupling layer to achieve high quality ultrathin films. To determine the appropriate NM layer for epitaxial growth of $CoFe_2O_4$, I fabricated Fe/NM(Cr, Au, Pt)/$CoFe_2O_4$ multilayers and examined their surface morphologies. The substrate temperature (T_{sub}) during $CoFe_2O_4$ deposition and the annealing temperature (T_a) were 300°C, which were relatively low to prevent diffusion at the interface at a high temperature.

Figure 2(a) presents the RHEED pattern of $CoFe_2O_4$ on Cr with thermal oxidation, where the electron beam was incident along the [100] direction. A streak RHEED pattern can be observed in Fig. 2(a), indicating the epitaxial growth of the $CoFe_2O_4$ film. The

lattice constants of Cr (0.288 nm) and Fe (0.287 nm) were almost the same, and the lattice mismatch between the $CoFe_2O_4$ and Cr layers was 3.12% (see Table 1). Figure 2(b) presents an AFM image of the $CoFe_2O_4$ on Cr after annealing. The roughness average, R_a, was 0.87 nm; however, large holes with diameters of 100 nm and depths of 7 nm were observed. Because the holes were deeper than the thickness of the $CoFe_2O_4$ layers, the Cr layers were considered to be oxidized or damaged during the thermal oxidation.

Figures 2(c) and (d) present the RHEED patterns and AFM images of $CoFe_2O_4$ on the Au layer with thermal oxidation. The electron beam was incident along the [100] direction. Figure 2(c) reveals a spotty pattern, indicating that the $CoFe_2O_4$ layer had a rough surface, although the Au/$CoFe_2$ before thermal oxidation exhibited a streak pattern. The Au lattice mismatch with the Fe layer was 0.52%, and the $CoFe_2O_4$ lattice mismatch with the Au layer was 3.19%. The surface of $CoFe_2O_4$ on Au contained many bumps, as observed in Fig. 2(d). The bumps were 150 nm wide and 6–7 nm high. The R_a of $CoFe_2O_4$ on Au was estimated to be 1.30 nm, which was larger than that of $CoFe_2O_4$ on Cr.

Figures 2(e) and (f) present the RHEED patterns and AFM images of $CoFe_2O_4$ on the Pt layer with thermal oxidation. The electron beam was incident along the [100] direction. Figure 2(e) reveals a slightly spotty pattern, which indicates that the surface was slightly rough. The RHEED patterns of Pt and $CoFe_2$ before thermal oxidation were streak patterns. The Pt lattice mismatch with the Fe layer was −3.42%, and the $CoFe_2O_4$ lattice mismatch with the Pt layer was 7.14%. For the surface of $CoFe_2O_4$ on Pt, no holes or bumps were observed in the AFM image, indicating a better surface than those in the Cr and Au cases. The R_a value was estimated to be 0.45 nm. The step heights on the surface

were approximately 1.6 nm, which is twice the lattice constant of $CoFe_2O_4$ (0.84 nm).

Table 1 Calculations of lattice mismatch

Non-magnetic metal (NM)	Lattice constant (nm)	Fe/NM (%)	NM/$CoFe_2O_4$ (%)
Cr	0.287	0.35	3.12
Au	0.408	0.52	3.19
Pt	0.392	−3.42	7.14

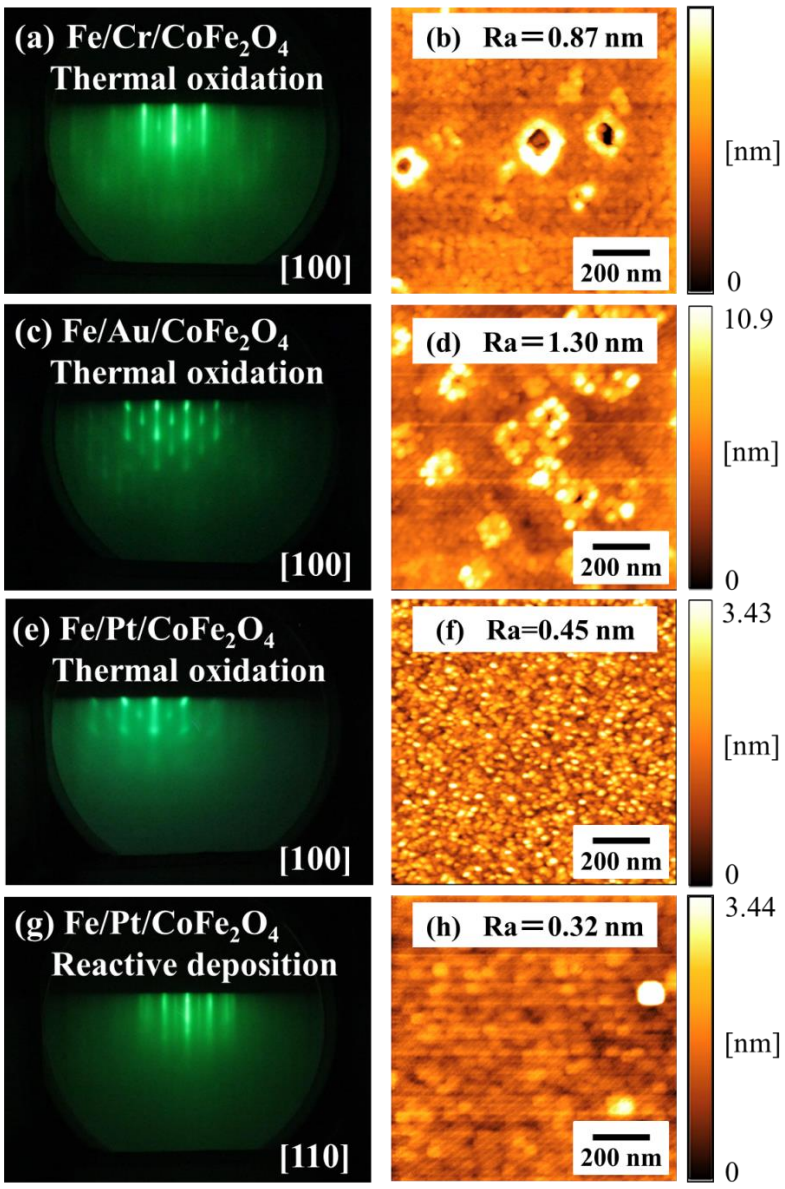

Fig. 2. RHEED patterns and AFM images of epitaxial $CoFe_2O_4$ films. The RHEED patterns of (a), (c), and (e) were taken after thermal oxidation at 300°C for 30 min. The AFM images in (b), (d), and (f) were obtained after thermal oxidation. (a) and (b) represent MgO(001)/Fe/Cr (2 nm)/$CoFe_2O_4$ (6 nm). (c) and (d) represent MgO(001)/Fe/Au (2 nm)/$CoFe_2O_4$ (10 nm). (e) and (f) represent MgO(001)/Fe/Pt (2 nm)/$CoFe_2O_4$ (5 nm). (g) and (h) MgO(001)/Fe/Pt (2 nm)/$CoFe_2O_4$ (5 nm) after reactive deposition.

As Pt appeared to be a good candidate as an NM layer, I fabricated $CoFe_2O_4$ on the Pt layer with reactive deposition in an oxygen radical of 4.0×10^{-4} Pa to determine the possibility of improving the surface roughness based on the oxidation conditions. Figures 2(g) and (h) present the RHEED pattern and an AFM image. The electron beam was incident along the [110] direction. A streak RHEED pattern and half-streak pattern are observed in Fig. 2(g). The R_a value in Fig. 2(h) was estimated to be 0.32 nm. The step heights were approximately 0.8 nm, which is equivalent to the lattice constant of $CoFe_2O_4$. These results indicate that the $CoFe_2O_4$ layer on Pt with reactive deposition was the optimal MI/NM layer material in our experiments. Because the Pt mixes easily with Fe at 350°C [17], T_{sub} and T_a were maintained at 300°C in this study, which were sufficiently lower than 350°C.

The RHEED patterns and AFM images of sample (2) are presented in Fig. 3. From the viewpoint of epitaxial growth, Pt is suitable for use as the NM in sample (1). However, Pt has been reported to have a short spin-diffusion length due to a large spin-orbit interaction[18] that could disturb the spin-current flow in the devices. Therefore, for sample (2), I employed the Cr layer as the NM layer, which has a smaller spin-orbit interaction than that of Pt. As described above, when the oxide was fabricated on the Cr layer by thermal oxidation as in sample (1), the Cr layer was damaged during the oxidation. In contrast, in sample (2), the Cr layer was grown on the oxide, and there was no oxidation process after the Cr growth. Therefore, oxidation of the Cr layer is considered to be significantly suppressed. Figures 3(a) and (b) present the RHEED patterns and AFM images of Fe_3O_4 grown on TiN. The electron beam was incident along the [100] direction. A clear streak pattern was observed for the as-deposited films. The R_a value of Fe_3O_4 was 0.34 nm, as shown in Fig. 3(b). The crystal grains were 50–100 nm

in diameter, and their heights were ~2.4 nm, corresponding to three times the Fe_3O_4 lattice constant. Therefore, the MgO barrier on this layer could have some roughness.

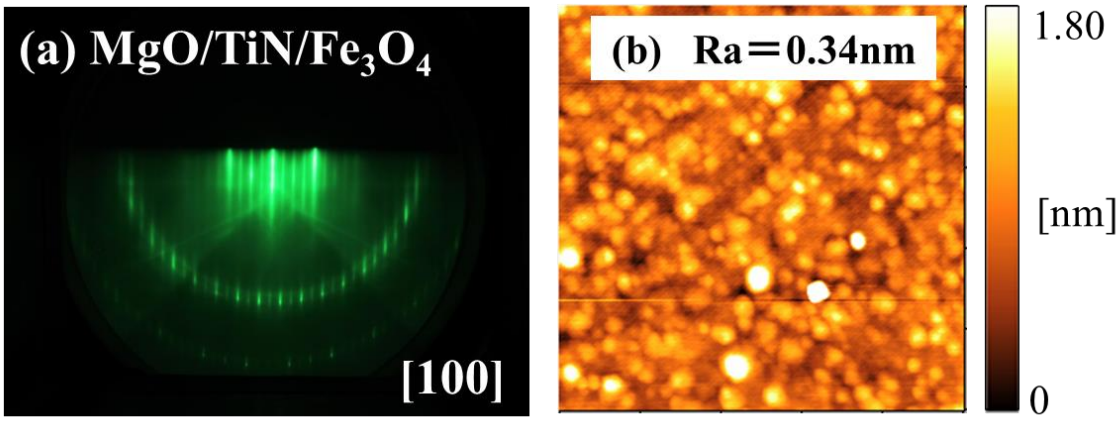

Fig. 3. RHEED patterns and AFM images of epitaxial MgO(001)/TiN(50 nm)/Fe_3O_4(60 nm). The RHEED pattern of (a) was taken after deposition at 300°C. The AFM image in (b) was obtained after deposition.

4.3.2. Magneto-transport Properties of the MTJs with Ferrite Layers

I fabricated the MTJs of samples (1) and (2) and measured their I–V characteristics in zero magnetic field, as shown in Fig. 4. The size of each junction in samples (1) and (2) was 300 × 150 nm^2 and 200 × 100 nm^2, respectively. Nonlinear I–V characteristics due to tunnel transport and a TMR ratio of 74% at 10 mV at RT for sample (1) were observed, as shown in Fig. 4(a) and (c). The resistance–area product (RA) was 532 $\Omega\mu m^2$, which was slightly less than that of conventional MgO–MTJs[1] despite the insertion of the $CoFe_2O_4$ layer. Although bulk $CoFe_2O_4$ is reported to be an insulator, the ultra-thin $CoFe_2O_4$ layer could be conductive because of oxygen vacancies or grain boundaries. The barrier height and width were estimated to be 0.32 eV and 1.47 nm, respectively, by

fitting the I–V characteristics with Simmons' equations [19]. The barrier height matched the reported value for conventional MgO–MTJs[1], whereas the barrier width was smaller than that of the MgO barrier in sample (1). The reason for this discrepancy is unclear thus far; however, it might be due to the fluctuations in the MgO thickness. The TMR curve had a high squareness, indicating that the $CoFe_2O_4$ layer did not magnetically affect the Fe/MgO/Fe junctions. I confirmed that the $CoFe_2O_4$ exhibited no abrupt switching of magnetization in the magnetic field for the MR measurement, which could be attributed to the anti-phase boundary[10] or magnetic anisotropy[20].

Sample (2), which had a MgO barrier of 1.5 nm, exhibited nonlinear I–V characteristics, indicating tunneling transport and an RA of 73 $\Omega\mu m^2$, as shown in Figs. 4(b) and (c). The RA value was comparable to that of conventional MgO–MTJs. Using Simmons' formula fitting, the barrier height and width were estimated to be 0.34 eV and 1.13 nm, respectively. The barrier width was less than the designed barrier thickness. The TMR ratio was 50% in Fig. 4, which was smaller than that of conventional MgO–MTJs. Such a small effective barrier thickness and TMR ratio could be attributed to the thickness fluctuation of MgO because MgO–MTJ was deposited on the rough surface of the Fe_3O_4 layer. The TMR curve for sample (2) exhibited a lower squareness than that for sample (1). The dipole interaction between the magnetic layers could be responsible for the low squareness[21].

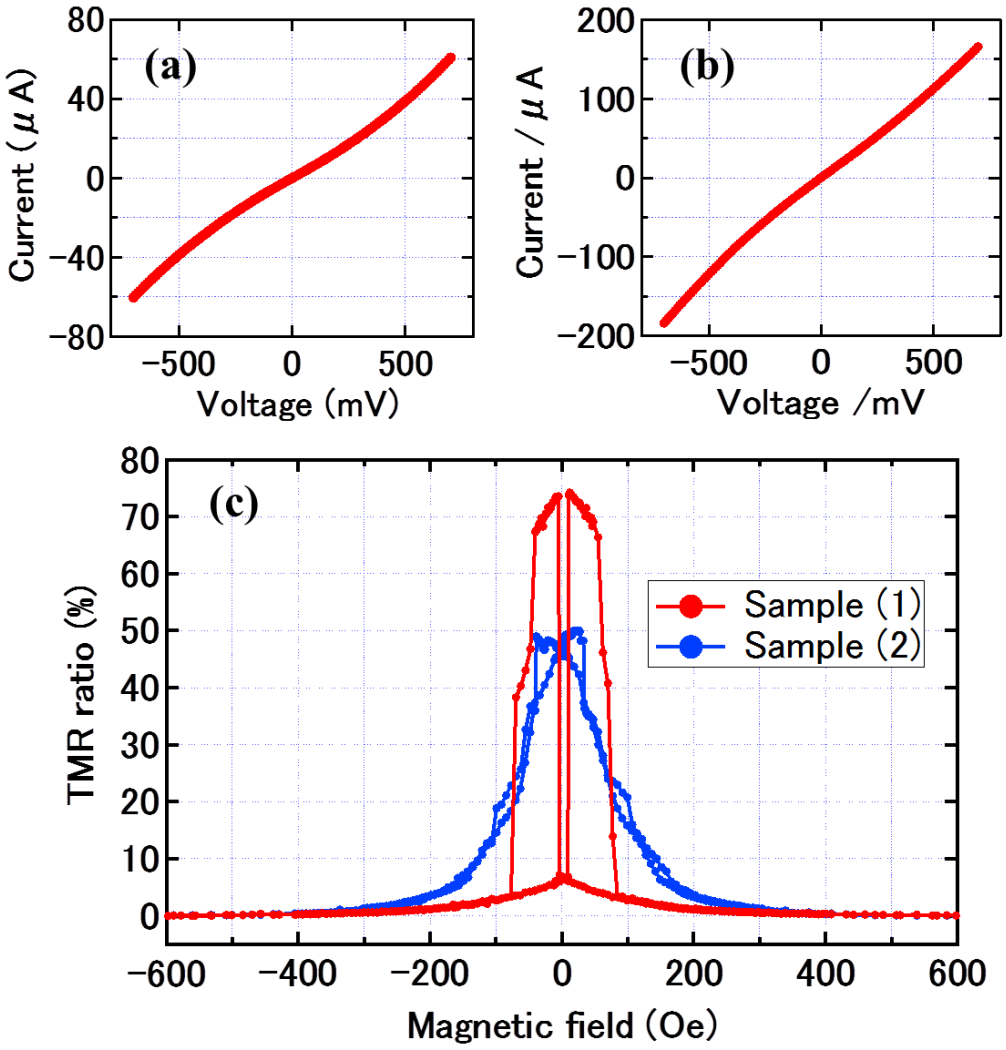

Fig. 4. Magneto-transport properties of the MTJs with ferrite layers. (a) and (b) are I–V characteristics for sample (1) and (2), respectively, at room temperature. The junction sizes are (a) 300 × 150 nm^2 and (b) 200 × 100 nm^2. The MgO thicknesses were (a) 2.0 nm and (b) 1.5 nm. (c) Magnetoresistance curves for samples (1) and (2) at room temperature with a bias voltage of 10 mV. The red and blue lines represent samples (1) and (2), respectively.

4.4. Conclusions

In summary, I fabricated the MTJs of (1) MgO(100)/MgO–MTJ/Pt/$CoFe_2O_4$ and (2) MgO(100)/Fe_3O_4/Cr/MgO–MTJ and investigated their epitaxial growth and magneto-transport properties. Pt was considered appropriate as the decoupling layer between Fe and ferrite layers in sample (1) from the viewpoint of epitaxial growth. Sample (1) exhibited TMR effects of 74% in terms of the magneto-transport properties. A TMR ratio of 50% was similarly observed in sample (2). The shape of the TMR curve strongly depended on the multilayer structure most likely because of the surface roughness and dipole interactions.

References

[1] S. Yuasa, T. Nagahama, A. Fukushima, Y. Suzuki, and K. Ando, Nat. Mater. **3**, 868–871 (2004).

[2] S. S. Parkin, C. Kaiser, A. Panchula, P. M. Rice, B. Hughes, M. Samant, and S. H. Yang, Nat. Mater. **3**, 862–867 (2004).

[3] K. Uchida, S. Takahashi, K. Harii, J. Ieda, W. Koshibae, K. Ando, S. Maekawa, and E. Saitoh, Nature (London) **455**, 778 (2008).

[4] A. A. Serga, A. V. Chumak, and B. Hillebrands. J. Phys. D: Appl. Phys. **43**, 264002 (2010).

[5] J. C. Slonczewski, Phys. Rev. B **82**, 054403 (2010).

[6] J. S. Moodera et al. J. Phys.: Condens. Matter **19**, 165202 (2007).

[7] Y. Suzuki, G. Hu, R. B. van Dover, R. J. Cava, J. Magn. Magn. Mater. **191**, 1–8 (1999).

[8] S. Xie, J. Cheng, B. W. Wessels, and V. P. Dravid, Appl. Phys. Lett. **93**, 181901 (2008).

[9] F. Rigato, J. Geshev, V. Skumryev, and J. Fontcuberta, J. Appl. Phys. **106**, 113924 (2009).

[10] D. Margulies, F. Parker, M. Rudee, F. Spada, J. Chapman, P. Aitchison, and A. Berkowitz, Phys. Rev. Lett. **79**, 5162 (1997).

[11] T. Nagahama, H. Kubota, and S. Yuasa, Thin Solid Films **519**, 8239–8242 (2011).

[12] T. Nagahama, Y. Matsuda, K. Tate, T. Kawai, N. Takahashi, S. Hiratani, Y. Watanabe, T. Yanase, and T. Shimada, Appl. Phys. Lett. **105**, 102410 (2014).

[13] K. Matsuzaki, H. Hosono, and T. Susaki, Appl. Phys. Exp. **6**, 073009 (2013).

[14] M. Mizuguchi, Y. Suzuki, T. Nagahama, and S. Yuasa, Appl. Phys. Lett. **88**, 251901 (2006).

[15] Y. K. Takahashi, S. Kasai, T. Furubayashi, S. Mitani, K. Inomata, and K. Hono, Appl.

Phys. Lett. **96**, 072512 (2010).

[16] H. Yanagihara, K. Uwabo, M. Minagawa, E. Kita, and N. Hirota, J. Appl. Phys. **109**, 07C122 (2011).

[17] W. R. Leibbrandt, R. van Wijk, and F. H. P. M. Habraken, Phys. Rev. B **47**, 11 (1992).

[18] J. Bass and W. P. Pratt, J. Phys. Condens. Matter 19(18), 183201 (2007).

[19] J. G. Simmons, J. Appl. Phys. **34**, 1793 (1963).

[20] H. Yanagihara, Y. Utsumi, T. Niizeki, J. Inoue, and Eiji Kita, J. Appl. Phys. **115**, 17A719 (2014).

[21] H. Kubota, G. Reiss, H. Brückl, W. Schepper, J. Wecker, and G. Gieres, Jpn. J. Appl. Phys. **41**, L180–L182 (2002).

Chapter 5
General conclusions

This thesis mainly consists of two parts. One is the experimental part of the Fe_3O_4 on Si substrate by molecular beam epitaxy method (Chapter 2 and 3). The other is the experimental part of magnetic tunnel junction including spinel ferrite materials (Chapter 4). The main results are summarized as follows.

In chapter 2, I fabricated an epitaxial Fe_3O_4 film on a Si substrate by inserting an γ-Al_2O_3 buffer layer. From the XRD measurement and TEM observation, the γ-Al_2O_3 buffer layer contributed to the growth of epitaxial Fe_3O_4(111) on Si(111). In contrast, the Fe_3O_4 film on an amo-Al_2O_3 buffer layer had an (111)-orientation with a textured structure. The Fe_3O_4 on γ-Al_2O_3 had magnetic properties corresponding to the bulk Fe_3O_4, furthermore the resistivity exhibited a Verwey transition at 120 K. The results indicate that the heterostructure of Si substrate / γ-Al_2O_3 / Fe_3O_4 could be used as a part of magnetic tunnel junctions or spin injection devices and will allow us to integrate spintronic devices including Fe_3O_4 electrode, e.g., spin-FET or magnetic tunnel junctions, on Si.

In chapter 3, I fabricated the magnetic tunnel junctions of the Fe_3O_4 / amo-Al_2O_3 / Fe on Si(111) substrate and investigated their epitaxial growth and magneto-transport properties. The crystal grain of Fe_3O_4 was improved in flatness by reducing the film forming rate. In addition, the TMR ratio was 2.4%, which is different from the conventional TMR ratio of negative. It was considered to be due to the existence of oxygen vacancies and pinholes in the amo-Al_2O_3 barrier, and that of anti-phase boundaries in

the Fe_3O_4 electrode by TEM observation.

In chapter 4, I fabricated the MTJs of (1) MgO(100) / MgO–MTJ / Pt / $CoFe_2O_4$ and (2) MgO(100) / Fe_3O_4 / Cr / MgO–MTJ and investigated their epitaxial growth and magneto-transport properties. Pt was considered appropriate as the decoupling layer between Fe and ferrite layers in sample (1) from the viewpoint of epitaxial growth. Sample (1) exhibited TMR effects of 74% in terms of the magneto-transport properties. A TMR ratio of 50% was similarly observed in sample (2). The shape of the TMR curve strongly depended on the multilayer structure most likely because of the surface roughness and dipole interactions.

In this thesis, I have opened up the research using a magnetic oxide thin film with spinel structure on a silicon substrate. In addition, I obtained one finding concerning the magnetic coupling of multilayer among three magnetic layers. It will bring about new research and development using the magnetic oxide thin film with spinel structure on silicon substrates.

Appendix

Publications related to this thesis

[1] Nozomi Takahashi, Tomohiro Kawai, Takashi Yanase, Toshihiro Shimada, and Taro Nagahama: "Investigation of epitaxial growth and tunnel magnetoresistance effects in magnetic tunnel junctions including spinel ferrite layers", Jpn. J. Appl. Phys. 54, 118003 (2015).

[2] Nozomi Takahashi, Teodor Huminiuc, Yuta Yamamoto, Takashi Yanase, Toshihiro Shimada, Atsufumi Hirohata, and Taro Nagahama: "Fabrication of Epitaxial Fe_3O_4 Film on a Si(111) Substrate", Scientific Reports 7, 7009 (2017).

Publications related to other research

[1] Taro Nagahama, Yuya Matsuda, Kazuya Tate, Shungo Hiratani, Yusuke Watanabe, Tomohiro Kawai, Nozomi Takahashi, Takashi Yanase, Toshihiro Shimada: "Magnetic properties of epitaxial Fe_3O_4 films with various crystal orientations and TMR effect in room temperature", Appl. Phys. Lett. 105, 102410 (2014).

[2] K. Omori, T. Kawai, N. Takahashi, T. Yanase, T. Shimada, and T. Nagahama: "The magnetic properties of Fe_3O_4/nonmagnetic metal/Fe hybrid systems", Appl. Phys. Lett. 110, 212402 (2017).

[3] Yuki Goto, Masato Araki, Nozomi Takahashi, Takashi Yanase, Toshihiro Shimada, Masahito Tsujikawa, Masafumi Shirai, Akira Kamimaki, Satoshi Iihama, Shigemi Mizukami, and Taro Nagahama: "Synthesis of metastable B2-type Fe–Sn alloy epitaxial films and study of their magnetic properties", Jpn. J. Appl. Phys. 57, 120302 (2018).

Acknowledgements

I would like to thank my supervisor Associate Professor Taro Nagahama for his thoughtful discussions, support, and guidance from the early stage of this research. I sincerely feel that any achievements are due to his continuing support.

I gratefully acknowledge Professor Toshihiro Shimada and Professor Atsufumi Hirohata (the University of York) for his valuable discussion, advice and sincere encouragement over the year. I am sure that his advice and discussion improved this works.

Likewise, I am grateful to Assistant Professor Takashi Yanase for his support and encouragement.

I want to thank all the students of the Laboratory of Solid State Chemistry, who had helped my daily work.

Finally, I want to thank my parents for their support and generous encouragement.

Nozomi Takahashi